THE QMAP AND MAT/TOCO EXPERIMENTS FOR MEASURING ANISOTROPY IN THE COSMIC MICROWAVE BACKGROUND

A. Miller[1,2,3], J. Beach[1,13], S. Bradley[1], M. J. Devlin[4,14], R. Caldwell[1,4,12], H. Chapman[4], W.B. Dorwart[1], T. Herbig[1,2,5], D. Jones[4], G. Monnelly[1,6], C. B. Netterfield[1,7], M. Nolta[1], L. A. Page[1], J. Puchalla[4,8], T. Robertson[1,10], E. Torbet[1,9], H. T. Tran[1] W. E. Vinje[1,11]

Subject headings: Cosmology: Cosmic Microwave Background Anisotropy: Instruments

Submitted to The Astrophysical Journal

ABSTRACT

We describe two related experiments that measured the anisotropy in the cosmic microwave background (CMB). QMAP was a balloon-borne telescope that flew twice in 1996, collecting data on degree angular scales with an array of six high electron mobility transistor-based amplifiers (HEMTs). QMAP was the first experiment to use an interlocking scan strategy to directly produce high signal-to-noise CMB maps. The QMAP gondola was then refit for ground based work as the MAT/TOCO experiment. Observations were made from 5200 m on Cerro Toco in Northern Chile in 1997 and 1998 using time-domain beam synthesis. MAT/TOCO was the first experiment to see both the rise and fall of the CMB angular spectrum, thereby localizing the position of the first peak to $l_{peak} = 216 \pm 14$. In addition to describing the instruments, we discuss the data selection methods, checks for systematic errors, and we compare the MAT/TOCO results to those from recent experiments. We also correct the data to account for an updated calibration and a small contribution from foreground emission. We find the amplitude of the first peak for $160 < l < 240$ to be $\delta T_{peak} = 80.9 \pm 3.4 \pm 5.1 \ \mu$K, where the first error is statistical and the second is from calibration.

1. INTRODUCTION

Experiments aimed at measuring the anisotropy in the CMB require a combination of sensitive detectors and novel observing strategies. The observational goal is to measure micro-Kelvin celestial variations in thermal emission with a telescope observing from an environment that is some ten million times brighter. Below 90 GHz, the detectors of choice have been high electron mobility transistor based amplifiers designed at NRAO [HEMTs, Pospieszalski (1992)]. Above 90 GHz, bolometers are the best detectors [e.g., (Bock *et al.* 1998; Lee *et al.* 1996; Downey *et al.* 1984; Tucker 1991)]. SIS-based systems (Kerr *et al.* 1993) near 100 GHz have the speed and intrinsic sensitivity of transistor amplifiers though do not yet have the large instantaneous bandwidth of bolometers or HEMTs. Over the past five years, instruments have been designed for direct mapping of the CMB [e.g., QMAP, BOOMERanG

(Piacentini *et al.* 2001), MAXIMA (Hanany *et al.* 2000), TopHat (2001)], and for beam synthesis [Saskatoon (SK) (Wollack *et al.* 1997), MSAM (Fixsen *et al.* 1996), Tenerife/Bolo (Romeo *et al.* 2000), PYTHON (Coble *et al.* 1999), VIPER (Peterson *et al.* 2000)]. More recently, interferometers based on HEMT amplifiers have reported CMB anisotropy results [CAT (Baker *et al.* 1999), DASI (Leitch *et al.* 2001), IAC (Harrison *et al.* 2000), CBI (Padin *et al.* 2000)]. Though the primary data product of the interferometers and beam-synthesis experiments is the angular spectrum, data taken with these techniques can be turned into maps (e.g., Tegmark 1997). Conversely, there is always some filtering involved in the mapping experiments. A common element of these experiments is that they are limited by systematic error.

In this paper, we describe the instruments for the QMAP experiment and the Mobile Anisotropy Telescope

[1] Dept. of Physics, Princeton University, Jadwin Hall, Princeton, NJ 08544

[2] Hubble Fellow

[3] Dept. of Astronomy and Astrophysics, The University of Chicago, Chicago, IL 60637

[4] Dept. of Physics and Astronomy, The University of Pennsylvania, Philadelphia, PA 19104

[5] McKinsey & Co., 3 Landmark Square, Stamford, CT 06901

[6] MIT CSR, Bldg 37-524, 70 Vassar St. Cambridge MA, 02139

[7] Dept. of Astronomy, University of Toronto, Toronto, Ontario, M5S 1A7

[8] Dept. of Molecular Biology, Princeton University, Princeton, NJ 08544

[9] Dept. of Physics, University of California, Santa Barbara, CA 93106

[10] Dept. of Physics, University of California at Berkeley, Berkeley, CA 94720

[11] Neurobiology Program, University of California at Berkeley, Berkeley, CA 94720

[12] Dept. of Physics, 6127 Wilder Lab, Dartmouth College, Dartmouth, NH 03755

[13] Xerox Corporation, Palo Alto, CA 94304

[14] Sloan Fellow

on Cerro Toco (MAT/TOCO or TOCO for short). We supply the details necessary for assessing the quality of the data and reproducing the experimental method. QMAP is described in part in Devlin *et al.* (1998) and analyses of the data are presented in Herbig *et al.* (1998), de Oliveira-Costa *et al.* (1998, 1999), Xu *et al.* (2000), and Park *et al.* (2001). Balloon borne mapping experiments have a long history (Weiss 1980; Partridge 1995) though highly interlocking scan strategies over limited regions of sky are more recent (Staren *et al.* 1999; de Bernardis *et al.* 2000; Lee *et al.* 2001). QMAP, which flew twice in 1996, was the first of these to produce a "true map" of the CMB, complete with pre-whitening and full covariance matrices. QMAP was comprised of a focal plane array of three dual polarized HEMT channels with an angular resolution of roughly 0°.8. The beam array was steered on the sky by a large chopping flat.

TOCO used the QMAP gondola and receiver refit to work with a mechanical cooler instead of liquid cryogens. It also employed two SIS-based[15] 144 GHz detector systems to improve the resolution to 0°.2. TOCO employed the Saskatoon-style beam synthesis strategy (Netterfield *et al.* 1995) with eight independent detectors. Instead of observing near the NCP from Saskatoon, Canada, we observed near the SCP from the side of Cerro Toco in Northern Chile [16]. At 144 GHz, the atmospheric column density in Saskatoon is too large for anisotropy measurements; a high altitude site such as the Chilean Altiplano is required. TOCO operated for two seasons in 1997 and 1998. The primary results and short description of the instrument are given in Torbet *et al.* (1999) and Miller *et al.* (1999). The 0°.2 resolution allowed us to locate the first peak in the angular spectrum at $l \approx 212 \pm 14$ (Knox and Page 2000). In the context of the popular adiabatic CDM models, this shows that the universe is geometrically flat (Doroshkevich *et al.* 1978; Kamionkowski *et al.* 1994; Bond *et al.* 1994; Hu & White 1996; Cornish 2000).

2. OVERVIEW OF GONDOLA AND MOBILE ANISOTROPY TELESCOPE

The TOCO experiment is shown schematically in Figure 1[17]. The part of the figure containing the optics and receiver is the QMAP balloon gondola. The radar trailer, on which the gondola is mounted, has a separable magnesium base. Three legs hold the base off the trailer and stabilize it. When the telescope is transported, the legs are removed. The radar trailer has a 1.4 m diameter precision bearing on which is mounted a 2.5 cm thick flat plate that holds the gondola. The plate and gondola are rotated using an on-axis DC motor[18]. CMB observations are made with the telescope in a fixed position; a brake holds the telescope in place allowing the motor to be shut off during observations and preventing it from drawing large currents or oscillating as it seeks the target position in high winds. The motor has a 15 cm diameter hole in the center through which cables and refrigerator hoses pass from the inside of

the telescope to the outside. The compressor that runs the mechanical cryocooler is mounted on the trailer. The azimuth is instrumented with an absolute 17-bit encoder and a 20-bit resolver.

3. THE RECEIVER

Radiation from the sky enters the dewar through a 15.25 cm diameter vacuum window made of 0.56 mm polypropylene and is collected with corrugated feed horns as shown in Figure 2. Three aluminum baffles define the entrance aperture, one is attached to the 40 K cold plate, one is attached to the dewar just inside the vacuum window, and one is attached to outside of the dewar. Strips of aluminized Mylar connecting the cold feeds to the ambient temperature dewar block RF interference and reduce optical loading on the cold stage. To prevent the formation of frost on the window, warm air is passed through a volume in front of the vacuum window defined by a Saran Wrap-covered aluminum cone attached to the outside of the dewar.

Two NRAO SIS mixers are attached to the ≈ 4.5 K stage of the dewar and six HEMTs are attached to the 40 K stage, two with center frequencies of 31 GHz (in Ka band) and four with center frequencies of 42 GHz (in Q band). Warm amplifiers, bandpass filters, noise sources, and local oscillator for the SIS system are housed in a 293 K "backpack" attached to the outside of the dewar. The primary difference between the TOCO and QMAP receiver configurations is that QMAP used liquid cryogens and TOCO used a mechanical refrigerator to cool the HEMTs as well as the SIS mixers.

3.1. *The SIS Configuration*

The SIS configuration is shown in Figure 3. The mixers are coupled to the sky with conical corrugated feed horns. A round-to-rectangular transition at the base of the horn transforms the incoming signal to a single polarization which is added to a signal from the local oscillator using a 20 dB branch line coupler. The combined signals are fed into the SIS mixer block. A sliding backshort, connected to the outside of the dewar by a flexible shaft, is used to tune the SIS mixer, while cold, for optimal coupling. The SIS is biased through a bias T which allows transmission of the RF signal while blocking the DC bias voltage. An associated circuit controls and reads the current through and voltage across the SIS. The signal then comes out of the bias T, goes through a 20 dB 4-6 GHz isolator (P & H Labs) and into a cold C-band (3.95-5.85 GHz) HEMT amplifier with 33 dB gain, as diagrammed in Figure 3. The SIS, branch line coupler, bias T, and C-band HEMT amplifier were all designed and fabricated at the National Radio Astronomy Observatory (NRAO).

The output of the cold HEMT is carried on stainless steel semi-rigid coax from the cold stage to the backpack where it is amplified by a warm 44 dB RF amplifier, filtered through a 3.5-6.5 GHz filter and detected with a detector diode (Hewlett-Packard: ±0.2 dB flatness and a

---

[15] SIS stands for Superconductor-Insulator-Superconductor. The detecting element is a quasi-particle mixer (Tucker & Feldman 1985).

[16] The Cerro Toco site of the Universidad Católica de Chile was made available through the generosity of Prof. Hernán Quintana, Dept. of Astronomy and Astrophysics. It is near the ALMA site.

[17] The Nike Ajax radar trailer was donated to the University of Pennsylvania by Lucent Technologies.

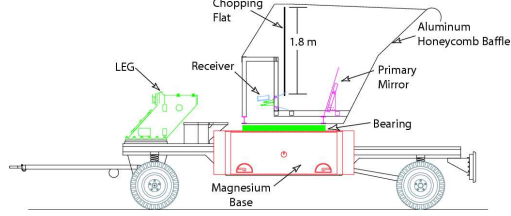[18] The motor is a Compumotor DR 1100A - 100 Nm torque.

FIG. 1.— Schematic of the Mobile Anisotropy Telescope. The legs are shown in their stowed position on the left end of the trailer. When observing, the compressor is also on the trailer. The QMAP gondola comprises everything above the bearing.
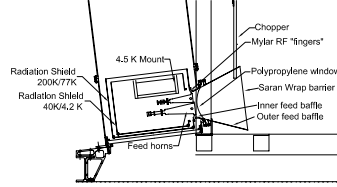

FIG. 2.— View of the inside of the dewar. Shown are the 4.5 K mounting structure, the thermal shield and cold plate at 40 K, and the shield at ≈ 200 K. In the QMAP configuration, the entire cold plate was cooled in the lab to 4.2 K with liquid Helium, or to ≈ 2.7 K in flight (≈ 33,000 m altitude). Pressure regulated LN$_2$ held the intermediate temperature stage near 77 K. The SIS mixers are mounted to the 4.5 K structure. There is a small section removed from the bottom of the chopper to accommodate the outer feed baffle. One source of modulated radiation is the cavity formed by the moving chopper and the feed baffle.
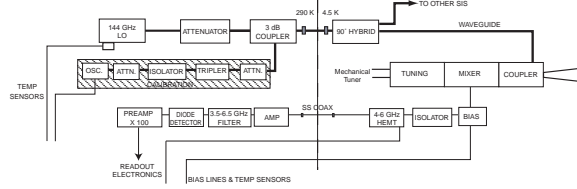

FIG. 3.— Components of the SIS Receiver. The components on the right are in the dewar. Components on the left are housed in the thermally stabilized 293 K backpack. The temperatures of all critical components are monitored.

typical sensitivity of 300 mV/mW). To increase the linearity and to bring the detector output into a convenient range (≈ 0.01 V), the diode is shunted with a ≈ 1 kΩ resistor. The RF filter ensures that only RF radiation in the passband of the C-band IF amplifier makes it through the system. The detected output is then amplified by 100 and sent to the data acquisition system. The IF system temperature was measured in the lab with a heatable 50 Ω load and found to be $T_{\rm sys}({\rm IF}) = < 6$K. The net gain of the system is 73 dB.

The LO (Millimeter Wave Oscillator Company) consists of a cavity stabilized oscillator with an output frequency of 48 GHz which injection-locks a second oscillator, which in turn injection locks a high power Gunn oscillator. The oscillator feeds a tripler with an output frequency of 144 GHz. This signal then goes through an attenuator, into a 3 dB directional coupler and is carried by WR-6 waveguide to the cold stage. On the cold stage a 90° hybrid splits the LO power and sends it to the two mixers. The third port of the coupler is used to couple test and calibration signals into the system. The total LO power is about 8.5 mW, ≈ 300 nW of which impinges on each SIS mixer.

3.2. *The HEMT Configuration*

Figure 4 shows the configuration of the HEMT receivers for the TOCO 1997 and 1998 observing seasons.

The QMAP configuration is almost identical. The radiation enters the dewar through the vacuum aperture described above and is collected using Ka- and Q-band corrugated horns. An orthomode transducer (OMT) splits the radiation into vertical and horizontal linear polarizations. The Ka-band OMT has a reflection coefficient of less than −26 dB over the bandpass of the channel. The Q-band OMTs have a reflection coefficient of less than −20 dB. Each polarization is carried by rectangular copper waveguide to a separate low noise NRAO cryogenic HEMT amplifier(Pospieszalski 1992; Pospieszalski *et al.* 1994). The passband of the system is set by the amplifiers and waveguide cutoff at the low end and a filter at the high end. Bends in the waveguide are limited to a radius of curvature of at least 1.5 cm in order to minimize reflections (Monnelly 1996).

At the input to each HEMT amplifier is a 20 dB crossed-guide Bethe hole coupler that is used to inject a noise pulse. There is one source for all four of the Q-band channels and one for both Ka-band channels.

Upon leaving the dewar, each of the Ka-band signals travels through waveguide to a warm amplifier. Ka2, the vertically polarized channel (Table 1), is amplified with a single warm amplifier with a gain of about 50 dB and a noise figure of 3-4 dB ($T_{sys} \approx 400$ K). The signal from Ka1, the horizontally polarized channel, was found to be com-
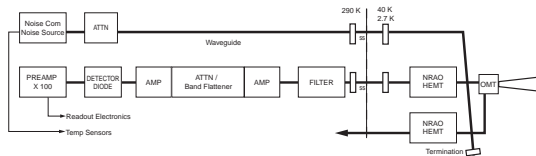
Fig. 4.— Components of a Q-band receiver, one of six HEMT radiometer channels. Components on the right are mounted to the 40 K (for TOCO, 2.7 K for QMAP) plate inside the dewar, and components on the left are in the 293 K backpack. The HEMT output is carried on a rectangular copper waveguide to the edge of the cold stage where it is connected to 0.5 m long thin walled stainless steel waveguide that runs down the vacuum chamber inside the dewar to warm stage. The stainless steel waveguide provides thermal isolation between the cold stage and ambient temperature. Copper waveguide from the ambient temperature end of the stainless steel segment runs to the vacuum seal which is formed with a piece of 0.013 mm thick kapton tape.

pressed in a similar configuration so it is passed through an amplifier (+29 dB), then through an attenuator (-12 dB) and through a second amplifier (also with +29 dB) before being detected with a diode. The net gain of the Ka receiver chains is ≈ 72 dB.

The Q-band signals, upon leaving the dewar, are carried via copper rectangular waveguide to 1 dB insertion loss filters (Spacek) that filters out the low frequency tail of the 60 GHz atmospheric oxygen line. Following the filters the signal is amplified, sent through a band leveler (designed individually for each channel by Pacific Millimeter) and amplified again. The amplifiers are connected to the band leveler with a K-connector to waveguide transition. Each amplifier has a gain of 26-28 dB and a noise figure of ≈ 4.5 dB. Tests of the system with and without the band levelers are discussed in Monnelly (1996). The net gain of each Q-band system is ≈ 75 dB.

A diode detector (Millitech) at the output of the final amplification stage of the HEMT channels converts the incident power to a voltage. The diode sensitivity varies over the passband and with temperature but is typically ≈ 2000 mV/mW. The output of the diode is connected to a low noise pre-amp with a typical gain of 100 and roughly 2 kΩ input impedance. We tune the DC output by selecting this impedance. Values vary by about a factor of 100 between different channels. The output of the pre-amp is buffered and sent to the data acquisition system.

3.3. Thermal, Mechanical, and Magnetic Considerations

In the QMAP configuration, the HEMT amplifiers and the SIS mixers are heat sunk to a cold plate that forms the bottom of the liquid helium reservoir. The outer tank of the dewar is filled with liquid nitrogen. The vapor pressures of both the nitrogen and helium are held at a constant value with mechanical regulators. The combination of pressure regulated cryogens and a balloon borne dewar produces a constant-temperature cold plate with minimal microphonics.

Due to the expense and difficulty of transporting liquid cryogens to Cerro Toco, the TOCO receiver is cooled with a Sumitomo cryogenic refrigerator (SRDK-408BA). The 40 K stage has 40 W of cooling power. The loading on the 40 K stage is dominated by HEMT LED's, waveguide connections between the cold and warm stages, and optical loading through the window. From the liquid cryogen boil-off rate in the QMAP configuration, we determined that the total loading on this stage is ≈ 20 W. The total loading on the 4 K stage, where there is 1 W of cooling power, is ≈ 400 mW.

In Chile, diurnal variations in the optical loading led

to variations in the temperature of the SIS mixers of ≈ 400 mK. However, for the purposes of CMB anisotropy analysis, we used only data taken during the night when the temperatures were stable to better than 50 mK. The temperatures were monitored continuously and the small drifts accounted for in the analysis through a calibration model. There was also a temperature variation of approximately 10 mK synchronous with the refrigerator drive motor operating at 1.2 Hz. This term is asynchronous with the chopping frequency, and the resulting gain fluctuations are too small to affect our results (Section 13).

The backpack that houses the warm electronics mounts on the dewar and is thermally controlled to within ± 0.5 K over a typical night of observations. As with the cold stage, the temperature is monitored continuously and the effects of drifts on gain are corrected in software. All microwave amplifiers are heat sunk to a common aluminum plate and their temperatures are monitored.

The enclosure for the electronics has two levels of RF shielding and is filled with pieces of microwave absorber wrapped in plastic bags that serve the dual purpose of thermal insulator and absorber of stray microwave radiation (perhaps from imperfect joints). All waveguide joints are wrapped with an absorber to prevent leakage of radiation into the rest of the system. We did not find any evidence for correlations between channels due to the instrument.

If changes in RF impedance due to vibrations are synchronously modulated by the motion of the chopping mirror, the resulting microphonic lines can mimic a celestial signal. Such "microphonics" can couple into the data, for example, through motion of the feeds or through strain in the microwave joints. If the coupling is large and variable, it can also affect the data even if it is asynchronous with the chopper.

In order to minimize this coupling, the cold head motor is vibrationally isolated from the dewar (which is bolted to the gondola frame) with a set of compensating flexible vacuum bellows. We also use bags of #9 lead shot placed on the cold head to damp vibrations. The connections between the cold head and the cooled electronics are made with strips of high purity flexible copper braid that efficiently conducts heat and vibrationally isolates the detectors from the refrigerator head.

Although microphonic levels were low at the beginning of the 1997 season, a microphonic coupling developed over the campaign that rendered the D-band data unusable for CMB observations. The coupling was manifest as 1.2 Hz (the cold head cycle) wings of a broad 90 Hz line suggest-

ing amplitude modulation of a 90 Hz vibrational line. The source of the vibration was traced to a combination of the azimuthal drive motor and the chopper. It was corrected for the 1998 season by modifying these two systems. The electronic interference from the azimuthal drive motor was eliminated by installing a brake. The brake allows the motor to be shut off during CMB observations and prevents large currents from being drawn by the motor working to counteract wind loading. In addition, the chopper-induced vibrations were reduced by replacing the bearings in the chopper with flex pivots. As a result, microphonic levels in the TOCO98 D-band data were negligible. Microphonics were not a problem either year in the HEMT data.

The Josephson junctions in the SIS mixers are sensitive to magnetic fields. Helmholz coils around the dewar were used to measure the dependence. With the coils absent, the area was mapped with a Gauss meter to ensure that the AC fields from the chopper drive and cold head motor would not contaminate the data. To minimize potential magnetic coupling, high magnetic permeability material (mu-metal) was wrapped around the outside of the chopper coils and around the cold head. Not only is the magnetic field negligible, but the chopper synchronous component corresponds to values of l that do not enter into the CMB analysis.

3.4. Receiver Characteristics

The QMAP/TOCO receiver was characterized in the lab before each campaign, but the most relevant characterizations are done while observing. We use the following definitions:

$$\nu_c = \frac{\int \nu g(\nu) d\nu}{\int g(\nu) d\nu} \qquad \Delta_n \nu = \frac{\left(\int g(\nu) d\nu\right)^2}{\int g^2(\nu) d\nu}. \qquad (1)$$

where g is the receiver passband, ν_c is the effective center frequency and $\Delta_n \nu$ is the noise bandwidth (Dicke 1946) for the radiometer equation.[19]

The noise of HEMT -based amplifiers has a $1/f$ characteristic (Jarosik 1996; Wollack 1995). To parametrize it, we fit the power spectrum of the detector diode output to the following form:

$$\tilde{T} = T_{sys}\sqrt{\frac{1}{\tau \Delta_n \nu} + f^\alpha} = T_{sys}\sqrt{\frac{1}{\tau \Delta_n \nu} + \left(\frac{\Delta G(f)}{G}\right)^2} \qquad (2)$$

where $\tilde{T}$ is the system sensitivity in units of K-sec$^{1/2}$, τ is the integration time, and $\Delta G/G$ is the fractional gain fluctuation that gives rise to the $1/f$ form. When the bandwidth is very large, the gain fluctuations dominate as shown by Wollack & Pospieszalski (1998). Note that a $1/f$ noise spectrum corresponds to $\alpha = -1$ in the variance ("power") of the detector output. We define the $1/f$ knee, f_{knee}, to be the frequency where the power spectrum (square of equation 2) increases by a factor of two over the value at high frequencies.

The instrument bandpasses, $g(\nu)$, are measured in the lab for each channel. Table 1 lists the center frequencies and effective noise bandwidths for each channel for each observing campaign as calculated from equation 1.

The SIS is operated in double side band (DSB) mode. By convention we use the intermediate frequency (IF) noise bandwidth in the radiometer equation and report "double sideband noise temperatures," T_{DSB}, because our source fills both RF bands. If a source fills just one RF band, a "single sideband noise," T_{SSB}, is reported. In an ideal system, $T_{DSB} = T_{SSB}/2$. We use the mean of the USB and LSB bandwidths for the noise bandwidth in the radiometer equation. A full calculation of the noise includes contributions from the mixer and the IF amplifier (Blundell 1992; Kerr et al. 1997); for our purposes we treat these as lumped elements.

3.4.1. SIS Sensitivity

Measurements of the SIS sensitivity have been made in several configurations as shown in Table 2. The values of $T_{\rm rec}$ from laboratory measurements are better than those made in the field. To investigate this discrepancy, we built an external cold load that could be bolted onto the front of the receiver to mimic the sky. We found that it was possible to approximately reproduce the system temperatures measured with the internal load using an external load provided that the tuning parameters were readjusted. This retuning compensates primarily for the change in temperature of the mixer. In the 1998 season, the combination of thermal loading and increasingly poor refrigerator performance led to an increase in the SIS temperatures and a temperature distribution different to that in the lab. Even though the system was tuned in the field, the lab performance was not duplicated.

The SIS system noise exhibits a $1/f$ characteristic presumably due to the C-band HEMT, though this has not been verified. The $1/f$ noise is parametrized following equation 2 in the last two lines of Table 2.

3.4.2. HEMT Sensitivity

The same set of six HEMT amplifiers were used for the two QMAP flights and the two observing seasons of the TOCO experiment; four of this set were used for the Saskatoon measurement. They were tested in the lab before each set of observations and the sensitivities were analyzed for each data set (Table 3). There is evidence of degradation in the HEMT performance between the QMAP and TOCO campaigns above that which is expected due to the difference in body temperature (Pospieszalski 1989). Generally HEMT system noise is expected to increase roughly one Kelvin for each Kelvin of increased ambient temperature. We suspect slow deterioration in the mechanics of the microwave/bias structures over the hundreds of cycles and sometimes rough handling these amplifiers experienced. The chips were unpassivated InP so there may some deterioration in the chip performance though this has not been confirmed.

4. OPTICS

The telescope optics are similar to those used in the Saskatoon experiment (Wollack et al. 1997). Corrugated feeds underilluminate a 0.86 m primary mirror which in turn underilluminates a flat (1.8 m×1.2 m) chopping mirror (chopper). Each of the eight channels detects a single mode of a diffraction limited beam. The chopper is

---

[19] Throughout the paper, we use ν for RF frequencies and f for audio (< 20 kHz) frequencies.

TABLE 1
CENTER FREQUENCY AND NOISE BANDWIDTHS FOR EACH CAMPAIGN.

| | QMAP | | TOCO 97 | | TOCO 98 | |
	ν_c (GHz)	$\Delta\nu$ (GHz)	ν_c (GHz)	$\Delta\nu$ (GHz)	ν_c (GHz)	$\Delta\nu$
Ka1	31.7 ± 0.3	4.7 ± 2.2	31.7 ± 0.3	4.7 ± 2.2	...	4.7^{*a}
Ka2	30.8 ± 0.2	6.2 ± 0.3	30.8 ± 0.2	6.2 ± 0.3	32.0 ± 0.1	8.8 ± 0.1
Q1	41.4 ± 0.2	6.9 ± 0.3	41.1 ± 0.2	6.9 ± 0.3	...	6.9^*
Q2	41.3 ± 0.2	7.5 ± 0.3	41.0 ± 0.2	7.3 ± 0.3	...	7.3^*
Q3	42.1 ± 0.2	6.3 ± 0.3	41.7 ± 0.2	6.3 ± 0.3	41.5 ± 0.1	5.3 ± 0.1
Q4	41.2 ± 0.2	7.0 ± 0.3	41.1 ± 0.2	4.6 ± 0.3	41.2 ± 0.1	4.5 ± 0.1
D1 (USB)	...	...	149.2 ± 0.2	2.9 ± 0.2	148.7 ± 0.1	2.3 ± 0.1
D1 (LSB)	...	...	138.3 ± 0.2	3.2 ± 0.2	139.4 ± 0.1	2.6 ± 0.1
D1 (DSB)[b]	...	...	141.8 ± 0.7	5.6 ± 0.4 (3.1)	143.7 ± 0.1	4.9 ± 0.1 (2.5)
D2 (USB)	...	...	148.7 ± 0.7	2.5 ± 0.4	148.6 ± 0.1	2.4 ± 0.1
D2 (LSB)	...	...	138.9 ± 0.7	1.7 ± 0.4	139.4 ± 0.1	2.8 ± 0.1
D2 (DSB)	...	...	145.4 ± 3.0	3.6 ± 1.3 (2.1)	143.3 ± 0.4	5.2 ± 0.1 (2.6)

[a]The * indicates that the bandwidth is assumed from the previous year.

[b]The D-band channels were not used in QMAP so no value is given. The SIS bandpasses were re-measured between 1997 and 1998 because they change with SIS tuning. The numbers in parentheses following the full RF bandwidths is the effective IF bandwidth for noise calculations.

TABLE 2
SIS SYSTEM PARAMETERS

	D1 (lab int.)	D1 (field)	(lab int.)	(field)
$T_{phys}(K)^a$	4.3	4.9	4.4	4.9
$V_B(mV)^b$	13.4	13.8	14.2	14.6
$\tilde{T}_{DSB}(mK\sqrt{s})^c$	0.6	1.3	0.7	1.2
$T_{sys}{}^d$	30	65	...	61
$T_{rec}{}^e$	26	48	...	44
$T_{rec}(y-factor)^f$	27	...	35	...
α	...	-1.0	...	-0.8
f_{knee} (Hz)	...	18	...	12

[a]The physical temperature of the SIS body. The uncertainty is $\approx \pm 0.2$ K. At $T > 5$ K the SIS sensitivity is markedly reduced.

[b]The optimal SIS bias voltage, V_B, across the 6 SIS junctions.

[c]The total power DSB sensitivity computed from the noise power spectrum at 200 Hz, where atmospheric fluctuations are negligible, and the responsivity. These are for a Rayleigh-Jeans source. In the field, the atmosphere and telescope contribute ≈ 17 K. In the lab, the load contributes ≈ 4 K. The loss from the feeds is measured to be negligible.

[d]The Rayleigh-Jeans system temperature computed from measured sensitivity and the noise bandwidth.

[e]The Rayleigh-Jeans receiver temperature computed from T_{sys}.

[f]The Rayleigh-Jeans receiver temperature measured with a variable temperature cryogenic load.

a resonant, computer controlled mirror, that scans in the azimuthal direction while the rest of the optics remain fixed in azimuth and elevation as the sky rotates through the beams. The telescope sits inside an aluminum ground screen which is fixed with respect to the primary mirror, the receiver, and the chopper mount.

4.1. The focal plane

Conical corrugated feed horns receive radiation from the sky and transform the incident fields so they may propagate through waveguide. All of our feeds were fabricated by Custom Microwave from electroformed copper over an aluminum mandrel. They are gold coated to stabilize the surface. The general electromagnetic design follows the guidelines in Clarricoats and Olver (1984) and MacA Thomas (1978). The throat section, where the corrugations adiabatically transform from $\lambda/2$ depth to $\lambda/4$ depth as the hybrid mode detaches from the feed wall, was designed by Wollack (1994) following the work of James (1982) [20] The VSWR is less than 1.05 across the waveguide band and the loss in the feed is negligible. We model the feeds with a commercial code (YRS Assoc.), CCHRN, that solves for the full electromagnetic field that propagates in the feed. Table 4 summarizes parameters of the feed horns

[20] In Ka band, the depths of grooves 1-10 are: 0.411, 0.368, 0.351, 0.335, 0.323, 0.312, 0.302, 0.292, 0.282, and 0.274 cm. This feed was designed by Ed Wollack.

TABLE 3

HEMT AMPLIFIER SYSTEM PARAMETERS

	QMAP[a]				TOCO 97[b]		TOCO 98			
	$T_{\rm sys}$	$\tilde{T}$	α	f_{knee}	$T_{\rm sys}$	$\tilde{T}$	$T_{\rm sys}$	$\tilde{T}$	α	f_{knee}
	K	mK$\sqrt{\rm s}$		Hz	K	mK$\sqrt{\rm s}$	K	mK$\sqrt{\rm s}$		Hz
Ka1	22	(0.40) 0.36	-1.2	62	89	1.3	162	(2.6) 2.4	-0.90	14
Ka2	23	(0.42) 0.32	-0.92	141	63	0.8	59	(0.9) 0.62	-0.85	95
Q1	17	0.21	...	...	91	1.1	84	(1.2) 1.0	-0.84	64
Q2	22	(0.60) 0.25	-0.82	686	145	1.7	114	(3.3) 1.3	-1.57	168
Q3	155	(2.1) 2.0	-0.78	20	63	0.8	80	(0.9) 0.72	-0.84	37
Q4	53	(0.85) 0.64	-0.71	67	156	2.3	88	(1.6) 1.3	-0.88	42

[a]From the first QMAP flight as shown in (Devlin *et al.* 1998). Q1 did not work during the flight so we report the lab measurements (Monnelly 1996). The four entries for each campaign correspond to the system temperature, the measured system sensitivity at 100 Hz (in parentheses) and very high frequencies, the gain fluctuation exponent, and the $1/f$ knee. In the fits to the power spectra, $f < 5$ Hz is not included. Because of the $1/f$ HEMT characteristics, $\tilde{T} = T_{sys}/\sqrt{\Delta_n \nu}$ is always smaller than the measured value of $\tilde{T}$ at 100 Hz. With the centroids in Table 1, the full noise spectrum may be recovered.

[b]From measurements in the field at 100 Hz.

TABLE 4

DESIGN PARAMETERS FOR ALL FEEDS

	Ka	Q1/2	Q3/4	D
Semiflare angle θ_o (deg)	6	4.4	5.4	5.4
Skyward aperture diameter d_h(cm)	4.2	2.0	2.1	0.89
OMT aperture diameter (cm)	0.833	0.650	0.650	0.173
Beamwidth $\theta_{\rm beam}^{\rm FWHM}$ (deg)	18	18	16	17
Phase error Δ (MacA Thomas 1978)	0.11	0.065	0.051	0.011
VSWR	1.03	1.03	1.03	1.05
Forward gain (dBi)	20.9	20.6	21.4	20.8
Number of corrugations	71	67	85	82
Length (cm)	19.3	12.0	14.5	3.96

used in the QMAP and TOCO experiments.

The Ka and Q1/2 feeds were also used in the Saskatoon experiments where they had three concentric choke grooves on the flange that defined the skyward aperture. It was believed that these would reduce "edge currents" resulting in a cleaner beam. To move the feeds as close together as possible in the focal plane, we removed those grooves and saw no degradation in performance.

Figure 5 shows a map of the beam pattern made by observing Jupiter. The feed horns are arranged so that the D-band beams with $0.2°$ resolution are placed as close to the center of the focal plane as possible. Beam parameters for each channel have been calculated and measured for each campaign as shown in Table 5.

Uncertainty in the beam solid angle leads to calibration uncertainty. Confidence in our understanding of the beams has been built by observing a variety of sources over two years and comparing those results with detailed models. QMAP mapped the beams using Cas-A and Saturn; TOCO mapped Jupiter more than 70 times. Each set of observations was independently fit. Variations from year to year are due to different alignments of the parabola and feeds.

4.2. Optical components

The primary mirror is a simple offset parabola. In the notation of Wollack et al. (1993), the offset angle is $\Psi_P = 48°$, and the focal length is 0.9 m. The dewar views the parabola at an angle of $\Psi_D = 7°$ thus the zenith angle of the optical axis is $90° - \Psi_P + \Psi_D = 49°$. The diameter of the parabola in projection is 0.86 m. The rms surface tolerance is ≈ 15 μm.

The chopper design follows that described in Wollack (1997) with a few modifications. It is smaller and lighter than the Saskatoon chopper, measuring 1.8 by 1.2 m, and is driven at the resonant frequency of a flat steel spring plate (85 cm by 8.62 cm by 0.167 cm for TOCO98) attached at its middle to the chopper mount. The surface tolerance of the plate is ≈ 30 μm. The thickness of the spring plate is tuned for each campaign. The resonant system produces a sinusoidal sweeping pattern in azimuth that requires minimal drive power and produces minimal vibrations on the mount. There is no reaction bar on the QMAP/TOCO chopper.

The chopper position is sensed 80 times per chop with a set of redundant LVDTs (Linear-Variable-Differential-Transformers), one on each side of the mirror. Errors in the sinusoidal chopper motion due to wind loading or instrument glitches are measured. The temperature of the chopper is monitored at all times using nine thermometers placed at various locations on the flat. For TOCO, when the rms chopper position over a single chop deviates from the expected position over the chop by more that $0°.015$ the data are rejected. The chopper zero point position in azimuth was measured as a function of time in the field and found to change less than $0°.01$. For QMAP, no data cuts were made based on the chopper motion.

5. OFFSETS AND SIDELOBES

Emission from the instrument produces signals that can potentially complicate the measurement[21]. We generically call these signals "offsets" as they are fairly constant over long periods and would be present in the absence of a celestial signal. Examples are shown in Figure 6. Outside of the data selection based on weather, most of the analysis effort goes into ensuring that offsets do not contaminate the final results. This section addresses the known offsets and sets upper limits on their magnitudes for both the case of when the source is chopper-modulated (radiation which enters the detectors after being affected by the chopper) and unmodulated (radiation which enters the detectors directly). The offsets from modulated emission can, in principle, occur at any harmonic of the chopper frequency[22]. In practice, they are predominantly at the lowest spatial frequency harmonics.

In the following we focus on TOCO because the long observing campaigns required careful monitoring of the offsets. In QMAP, because of the short durations of the flights, the offsets were stable. In the mapmaking analysis, the offsets were projected out of the CMB data using a technique described in de Oliveira-Costa et al. (1998).

5.1. Earth Emission Offset

Radiation from the Earth can diffract over the front edge of the ground screen and enter the receivers. The temperature of the ground as seen by the detectors is

$$T_A \approx \frac{g_{\text{feed}}(\theta)}{4\pi} \left[\frac{D^2}{r} \right] T_E \Omega_E \qquad \text{with} \qquad (3)$$

$$D = -\frac{\sqrt{\lambda}}{4\pi} \left[\frac{1}{\cos((\gamma - \alpha)/2)} \pm \frac{1}{\sin((\gamma + \alpha)/2)} \right] \quad (4)$$

where T_E is the physical temperature of the Earth (≈ 273 K); $g_{\text{feed}}(\theta)$ is the gain of the feed as defined by $G_{max}P_n(\theta)$ where G_{max} is the forward gain and $P_n(\theta)$ is the normalized beam pattern; Ω_E is the solid angle of the Earth subtended by the telescope rim; r is the distance from the horn to the top front edge of the baffle; γ and α are the diffraction angles; and D is the diffraction coefficient (Keller 1962). The positive sign in D is for the E-field perpendicular to the edge and the negative sign is for the E-field parallel to the edge.

From integrating equation 4 over the geometry of the ground screen and the feed pattern, we find the diffracted power in D-band into the feed $T_A \approx 25$ μK. The front baffle, which is in the far field of the feed, has a "Keller flare" that reduces the diffracted power over that from the sharp edge we assumed in the calculation. Based on our experience, calculations of this type involving complicated geometries are accurate to roughly a factor of three. We have included this factor in Table 6 where results are summarized.

We estimate the modulated contribution the same way as above but with $g_{\text{feed}}(\theta)$ replaced by $g_{\text{beam}}(\theta)$, the far-field gain of the main beam rather than the gain of the horn. The calculated power diffracted into the chopper sidelobes is ≈ 5 μK. The front baffle is in the near field

---

[21] The Sun is another source. For TOCO, the Sun travels overhead and so cannot be completely blocked at all times. However, for CMB work we use data only from when the Sun is fully blocked from the optics. QMAP flew at night. Lunar emission was not seen in either experiment.

[22] We use the term "harmonic" to refer to the spatial frequencies of the scan pattern as discussed in Section 10.

TABLE 5

BEAM PARAMETERS

Campaign	Ka1	Ka2	Q1	Q2	Q3	Q4	D1	D2
Predicted								
Ω_A[a] $(10^{-4}$ sr)	2.76	2.76	1.53	1.53	1.69	1.69	0.124	$\cdots$
θ_{FWHM}^{az}[b] (deg)	0.905	0.905	0.663	0.663	0.702	0.702	0.190	$\cdots$
θ_{FWHM}^{el}[b] (deg)	0.888	0.888	0.661	.661	0.683	0.683	0.192	$\cdots$
Azimuth[c] (deg)	203.13	203.13	206.75	206.75	206.70	206.70	205.00	$\cdots$
Elevation (deg)	41.8	41.8	41.8	41.8	39.2	39.2	40.66	$\cdots$
Polarization	$\leftrightarrow$	$\updownarrow$	$\leftrightarrow$	$\updownarrow$	$\leftrightarrow$	$\updownarrow$	$\leftrightarrow$	$\updownarrow$
Pri ET (dB)[d]	-21	-21	-19	-19	-20	-20	-22	$\cdots$
Chop ET (dB)	-47	-47	-48	-48	-49	-49	-54	$\cdots$
QMAP96a								
Ω_A $(10^{-4}$ sr)	2.83	2.83	1.58	1.58	1.62	1.62	$\cdots$	$\cdots$
θ_{FWHM}^{Maj} (deg)	0.931	0.931	0.694	0.694	0.700	0.700	$\cdots$	$\cdots$
θ_{FWHM}^{Min} (deg)	0.882	0.882	0.658	0.658	0.668	0.668	$\cdots$	$\cdots$
Cross-El (deg)	-1.35	-1.35	+1.35	+1.35	+1.35	+1.35	$\cdots$	$\cdots$
QMAP96b								
Ω_A $(10^{-4}$ sr)	2.67	2.67	1.43	1.43	1.75	1.75	$\cdots$	$\cdots$
θ_{FWHM}^{Maj} (deg)	0.932	0.932	0.674	0.674	0.730	0.730	$\cdots$	$\cdots$
θ_{FWHM}^{Min} (deg)	0.831	0.831	0.616	0.616	0.694	0.694	$\cdots$	$\cdots$
Cross-El (deg)	-1.35	-1.35	+1.35	+1.35	+1.35	+1.35	$\cdots$	$\cdots$
Elevation (deg)	41.36	41.36	41.37	41.37	38.79	38.79	$\cdots$	$\cdots$
TOCO97[e]								
Ω_A $(10^{-4}$ sr)	2.76	2.73	1.63	1.74	1.76	1.78	0.183	0.323
σ_Ω[g]	6%	6.5%	4%	8%	4%	6.0%	5%	6%
θ_{FWHM}^{az} (deg)	0.881	0.871	0.711	0.744	0.718	0.716	0.225	0.306
θ_{FWHM}^{el} (deg)	0.909	0.909	0.664	0.676	0.711	0.721	0.236	0.306
Azimuth (deg)	203.13	203.13	206.75	206.75	206.70	206.70	205.00	$\cdots$
Elevation (deg)	41.75	41.75	41.85	41.85	39.25	39.25	40.44	39.93
TOCO98								
Ω_A $(10^{-4}$ sr)	3.00	3.00	1.52	1.60	1.76	1.80	0.136[f]	0.292
σ_Ω	8%	8%	9.8%	18%	8.4%	10%	5.5%	5%
θ_{FWHM}^{az} (deg)	0.860	0.914	0.666	0.669	0.692	0.688	0.201	0.293
θ_{FWHM}^{el} (deg)	0.907	0.918	0.659	0.681	0.732	0.754	0.194	0.286
Azimuth (deg)	205.67	205.67	209.16	209.16	209.06	209.06	207.47	205.73
Elevation (deg)	42.05	42.05	42.03	42.03	39.48	39.48	40.63	40.13

[a] Solid angle of beam.

[b] The full width at half maximum in the azimuthal and elevation direction. The beam is not symmetric due to smearing in the azimuth direction and due to the placement in the focal plane. For QMAP, we give the major and minor axes of the best fit ellipsoidal Gaussian.

[c] The azimuth and elevation of the beams. For QMAP, we give the relative position in the focal plane. For TOCO98, the pointing was slightly different.

[d] The edge taper is the ratio of radiant power in the center of the optic to that on the edge expressed in dB. This is determined from a full calculation of the current distribution on each optical element using the DADRA program (YRS Assoc.).

[e] The chopper was tilted around its normal for TOCO97 and so the beam moved in elevation by $0.116\sin(\theta_{az-chop})$ deg. There was no tilt in TOCO98.

[f] The prediction is for the 1998 configuration. D band is also the most sensitive to slight changes in alignment.

[g] The rms in the solid angle during the campaign rounded to the nearest 0.5%.

Fig. 5.— Beam map of focal plane (left) and the synthesized beams (right). *Left:* Units are degrees on the sky from the center of the focal plane. Each beam is normalized with the contours representing 10% in amplitude. The physical separations between the Ka1/2 horn and the Q1/2 feed is ≈ 5 cm. D2 is offset from the focal plane center by 2.9 cm. The distance between the Q1/2 and Q3/4 feeds is also ≈ 5 cm. This is also a picture of the up/down reflection of the feeds in the focal plane when looking into the dewar. *Right:* The synthesized beams for TOCO97 as discussed in Section 10. If the Ka primary beam on the left, for example, is weighted by positive and negative numbers as it moves across the sky, one obtains the synthesized Ka pattern on the right. The contours indicate alternate positive and negative lobes. Shown are the Ka 9-pt, Q 11-pt, and D 27-pt D beams. From this picture, it is clear that the synthesized beam is sensitive to only a narrow band of spatial frequencies. The central dashed line corresponds to RA=0 (Fig. 8) though the synthesized beam location as shown is arbitrary. In the full analysis, the beam is smoothed in right ascension.

TABLE 6

ESTIMATED CONTRIBUTIONS TO THE OFFSETS

Contributions to the Signal	D-Band	Q-Band	Ka-Band	Modulated
Earth emission (directly into feed)[a]	75 μK	300 μK	400 μK	No
Earth emission (in chopper sidelobes)[b]	< 50 μK	< 200 μK	< 250 μK	No
Ground screen emission (directly into feed)	5 K	6 K	7 K	No
Ground screen emission (in chopper sidelobes)	80 mK	80 mK	80 mK	No
Cavity emission, vertically polarized	3 mK	13 mK	15 mK	No
Total loading from optics	5 K	6 K	7 K	
Total ground screen emission[c]	1.5 mK	1.5 mK	1.5 mK	Yes
Cavity emission (vertically polarized)[e]	0.3 mK	1.3 mK	1.5 mK	Yes
Polarized chopper emission[d]	3.5 mK	1.8 mK	1.6 mK	**Yes**
$\delta T_\parallel$ mirror misalignment in atmosphere	3 mK	1.7 mK	1.7 mK	**Yes**
$\delta T_\perp$ mirror misalignment in atmosphere	20 μK	10 μK	10 μK	**Yes**
Feed rotation (1°)	3 mK	0.8 mK	0.6 mK	**Yes**
Feed rotation (4°)	10 mK	3 mK	2 mK	**Yes**

[a]Results of the formal calculation times three to account for modeling errors.

[b]Includes a factor to account for near field effects.

[c]Due to a hypothetical temperature gradient across the ground screen.

[d]Magnitude of the largest component of polarized emission. The bold "**Yes**" indicates that this quantity is computed to 10% accuracy.

[e]We estimate that the effective area of the cavity between the chopper and the outer feed baffle is modulated by 10%.

of the main beam and so the true values could be up to an order of magnitude larger. If the temperature of the ground on either side of the telescope were to differ by 10 K then the offset produced would be < 1 μK. Similarly, any modulation of diffracted power from variations along the top of the ground screen are small. From these estimates we conclude that emission from the Earth does not contribute to the microwave signal.

5.2. *Ground Screen Emission Offset*

The antenna temperature from emission of the baffles as seen by the receiver is

$$T_A \approx \frac{g_{\text{feed}}(\theta)}{4\pi} \epsilon_{baffle} T_{\text{baffle}} \Omega_{\text{baffle}} \approx 5\text{K}. \qquad (5)$$

where ϵ_{baffle} is the emissivity of the baffle and T_{baffle} is its physical temperature. Along with the atmosphere, the direct emission from the ground screens is the largest radiation loading. As with the diffracted ground emission, we ask what portion of this signal is modulated. We find that the temperature of the baffle in the main beam, after reflecting off the chopper, is ≈ 80 mK. A temperature differential of 10 K on either side of the baffle would then translate to an observed offset of ≈ 1.5 mK in the lowest harmonics. It is also possible to get modulated emission because the polarized emission is a function of the angle of the beam with respect to the ground screen. The geometry of the enclosure is complicated, but the angle of the ground screen implies that the emission will be greatest in the vertical polarization. However, the modulation will be greatest for the horizontal component. This term is similar in character to the polarized emission from the chopper but is an order of magnitude smaller.

5.3. *Cavity Emission Offset*

The cavity behind the chopping mirror (Fig. 2)and outer feed baffle is effectively black. Radiation from this cavity reaches the receiver: a) by traveling over the front edge of the outer feed baffle and back into the feeds or b) through shallow angle diffraction over the outer feed baffle onto the parabola and then reflecting back to the feeds. This emission is modulated as the chopping mirror sweeps back and forth, changing the size and shape of the opening to the emitting cavity. Improved shielding of this cavity between the two QMAP flights reduced the offset at a given angle of the chopper by 1.8 mK or 50% in Ka band (Herbig *et al.* 1998).

The contribution from radiation traveling over the feed baffle and back into the feeds may be estimated with equation 4. For D-band we find that $T_A \approx 3$ mK for vertically polarized radiation and $T_A \approx 0.1$ mK for horizontally polarized radiation.

The contribution from the shallow angle diffraction is difficult to compute to even order-of-magnitude accuracy because it is so critically dependent on the geometry. We note, though, that this term can be of millikelvin magnitude and horizontally polarized.

5.4. *Chopper Polarized Emission Offset*

The emission from the chopping plate is polarized and depends on the angle of the mirror (Landau & Lifshitz 1960; Wollack *et al.* 1993 ;

Cortiglioni 1994). Therefore, as the chopping mirror scans across the sky the plate emissivity, as viewed by a feed, changes with the position of the chopper. The parallel and perpendicular emissivities are:

$$\epsilon_{\parallel} \approx \epsilon_0/\cos(\theta_i) \quad \& \quad \epsilon_{\perp} \approx \epsilon_0\cos(\theta_i), \qquad (6)$$

where ϵ_0 is the emissivity at normal incidence and the incident angle of radiation is

$$\theta_i(\phi_c) = \cos^{-1}[-\hat{k}_i \cdot \hat{n}(\phi_c)], \qquad (7)$$

where $\hat{k}_i$ is the propagation vector for the incoming ray, $\hat{n}$ is the normal to the plate, and ϕ_c is the chopper angle in the azimuthal direction. The brightness temperature of the plate is

$$T_{emit} \approx T_{chop}[\epsilon_{\parallel}|\tilde{E}_{\parallel}(\theta_i)|^2 + \epsilon_{\perp}|\tilde{E}_{\perp}(\theta_i)|^2], \qquad (8)$$

where $\tilde{E}_{\parallel}$ and $\tilde{E}_{\perp}$ are the parallel and perpendicular electric field projections onto the normal to the chopping mirror and T_{chop} is the physical temperature of the chopper. For the D-band, the peak-to-peak calculated offset is ≈ 3.5 mK. The dashed curves in Figure 6 show the polarized emission offset calculated for each of the channels.

In the beam synthesis, the net signal for each chopper position is multiplied by the corresponding element in the synthesis vector (Section 10). The offset, since it is an additive signal, is multiplied by the same vectors. It is evident from Figure 6 that the offset in the synthesized signal, or "synthesized offset," will be larger for the smaller harmonics. The polarization directions were chosen to minimize the synthesized offset for the 3-pt beam as no science data is expected from 2-pt beam.

5.5. *Atmospheric Offsets*

When the telescope is properly aligned, the chopper scans horizontally through the atmosphere and the atmospheric emission temperature at all portions of the chop is the same. If either the chopping mirror or the entire base is misaligned with respect to the horizontal, offsets are produced (Wollack *et al.* 1997) according to

$$T_{atm} = <T_{atm}> + \frac{\partial T_{atm}}{\partial \psi}\left[\delta\psi_{\parallel} + \delta\psi_{\perp}\right] \qquad (9)$$

where

$$\frac{\partial T_{atm}}{\partial \psi} = T_z\tan(\theta_z)\sec(\theta_z) \qquad (10)$$

is the gradient in the atmospheric temperature, T_z is the zenith temperature, and θ_z is the fiducial zenith angle of the beam. If the chopper is misaligned due to a rotation about an axis parallel to the chopper normal, the sky signal is changed by

$$\delta\psi_{\parallel} \approx 2\delta\theta_{\parallel}\sin(\theta_z)\sin(\phi_c) \qquad (11)$$

where ϕ_c is the azimuthal chopper angle. If the chopper is misaligned due to a rotation about an axis perpendicular to the chopper normal, the sky signal is changed by

$$\delta\psi_{\perp} \approx -2\delta\theta_{\perp}\cos(\theta_z)\cos(\phi_c). \qquad (12)$$

Measurements of chopper and base tilt put a limit on the measured value of $\delta\theta_{\parallel}$ and $\delta\theta_{\perp}$ of $\leq 0.1°$. Assuming this value, we would expect $\delta T_{\parallel} \approx 3$ mK and $\delta T_{\perp} \approx 20\mu$K for the D-band.
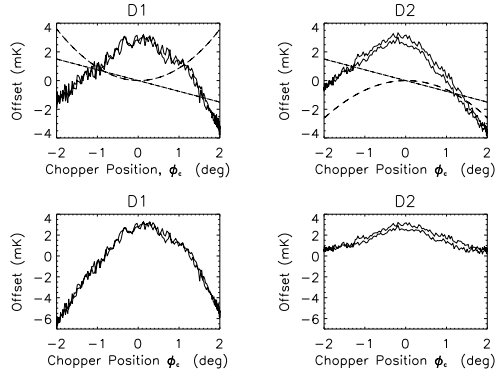
FIG. 6.— *Top Panels:* Measured chopper offsets, O_i, in D-band as a function of chopper position for a typical night of CMB data. This plot shows the raw data (with cal pulses subtracted) synchronously coadded with the chopper azimuth, ϕ_c. Dashed lines are the calculated offsets due to polarized emission from the chopping mirror with the offset at the center of the chop removed, $T(\phi_c) - < T(\phi_c = 0) >$. The straight lines are the calculated offset due to a mirror tilt of $\delta\theta_\| = 0°.1$ in the plane of the stationary chopper. When these offsets are multiplied by a synthesis vector, the result is constant in time and independent of chopper position. D1 is horizontally polarized; D2 is vertically polarized. *Bottom Panels:* The residual measured offset after the subtraction of the predicted offsets. The form of the residual indicates that the source is polarized. The asymmetry in D1 may be due to feed rotation.

5.6. *Observed Offset*

Figure 6 shows the chopper-position-dependent offsets observed in each of the D-band channels on a typical night analyzed for CMB observations in the 1998 campaign. Plotted in the top frames are the observed offsets (in antenna temperature) as a function of azimuthal chopper angle. Overplotted are the computed polarized emission offsets for each of the channels (dashed line) and offset due to mirror tilt about an axis parallel to the chopper normal (solid line). The bottom frames show the offsets corrected for these two effects.

There is a clear asymmetry in the offset about $\phi_c = 0$ in the top panels of Figure 6. This is most likely caused by a misalignment of the chopper with $\delta\theta_\| = 0.1°$ (equation 11), corresponding to the D-band beam centroid moving up and down vertically $\delta\Psi_\| = 0°.0053$ as it scans the azimuth. This angle is just below the detection threshold of our measurements (Section 7). With a zenith temperature of 10 K in D-band, $\delta\theta_\| = 0.1°$ produces a 1.6 mK modulation.

Another mechanism for producing an asymmetry of the same magnitude is the rotation of the polarization direction of a feed. A $\approx 1°$ rotation results in a signal of 3 mK in D-band (Table 6). We cannot rule out that some part of the asymmetry is due to this, though it would be coincidental to have the asymmetry so similar in both feeds. In the HEMT channels, the signature of the asymmetry due to feed rotation is opposite in the two polarizations. As the chopper sweeps, the emission for one polarization goes up while that from the other polarization goes down. We see no evidence for such a signal.

The offsets for Ka and Q band are similar to those shown in Fig. 6 and in Fig. 1 of Herbig *et al.* (1998). Before accounting for the chopper emission, the magnitude is between 4 to 8 mK. The offsets in Ka and Q bands in the Saskatoon experiment were 1/2 to 2 mK, considerably smaller than those observed here. We attribute the difference to the fact that the TOCO/QMAP system is, by necessity, much more compact: the chopper is closer to the feed horns and the ground screens are closer to the main beam.

After accounting for the polarized chopper emission and the alignment of the chopper, both of which can be computed accurately, there is still a residual polarized offset in all channels of magnitude 2 to 8 mK. In particular, the observed residual offset is always largest in the horizontal polarization as shown for D-band in the bottom panels of Fig. 6. The offsets are largest in Q-band, and thus no particular characteristic spectrum is identified. This suggests that the source is modulated cavity emission, thermal emission from the enclosure, or a combination of both. We have not been able to definitively identify the mechanism responsible for the effect though the most likely source is the shallow angle diffraction of the chopper cavity emission into the parabola. Other potential sources are either too small or do not have the correct polarization.

The offsets we discuss in this section are not atypical for CMB experiments. They correspond to the raw detector output before any of the symmetries or modulations of the experimental design have been utilized. In Sections 11 and 12 we discuss the offsets *after* the strong spatio-temporal filter of the experimental method has been applied.

6. ELECTRONICS AND DATA ACQUISITION

Because it was balloon borne, QMAP was by necessity self contained. It had its own command telemetry and CCD-based pointing system (Devlin *et al.* 1998) though used the National Scientific Balloon Facility (NSBF) transmitters to relay data. To operate remotely in Chile as the TOCO experiment, a transmitter was added to telemeter a compressed version of the data from the telescope on Cerro Toco to the ground station in San Pedro de Atacama, 35 km away. A block diagram of the telescope electronics, data system, and telemetry is shown in Figure 7.

6.1. *Electronics*

The eight radiometry signals are processed in the backpack. Each signal is square-law detected with detector diodes, amplified, and sent with differential line drivers to a processing board. On the processing board, the signal is high-pass filtered with a 2-pole RC network with $f_{3dB} = 1$ Hz to remove the DC level which is separately
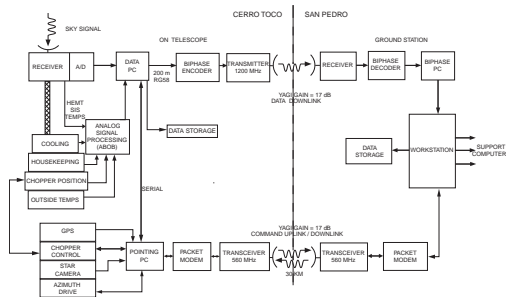
Fig. 7.— Layout of electronics and telemetry system for TOCO. The components on the left are on Cerro Toco and the ones on the right are at the ground station in San Pedro (a hotel room in La Casa de Don Tomás), at a comfortable living altitude. The command up/down link is a 40 W Motorolla GM300 radio communicating via a Paccomm packet modem.

recorded. This filter introduces a small but stable electronic offset. The high-passed analog signal is then digitized using an 18-bit $\Sigma\Delta$ analog to digital converter [23]. The serial digital signal is sent through a shift register and latch that converts it to a 32-bit parallel word accessible by a computer. The use of $\Sigma\Delta$ ADCs is advantageous over sampling ADCs because of their superior differential nonlinearity specification, which is important when signals comparable to or smaller than the 1-bit level are of interest. Additionally, these ADCs incorporate a digital anti-aliasing filter, eliminating any temperature dependence or drift in this component of the electronic band pass.

In the CMB analysis, we use HEMT data from 14 to 55 Hz ($4 < l < 200$) and SIS data from 15 to 60 Hz ($4 < l < 500$). The electronic bandpasses are defined on the lower end by the high-pass filter and on the high end by the $\Sigma\Delta$ chip. Over our frequency range, the phase response of the chip is linear with frequency and so the $\Sigma\Delta$ introduces a time delay in the signal. The amplitude response over the CMB frequencies varies by less than 0.4% over this range.

6.2. *Computers and Telemetry*

Two single board computers, which handle the data and the pointing, are located on the telescope. They are synchronized with a common clock and communicate remotely with the computers operating at the base station. In the following, we focus on the configuration for TOCO.

The "Data PC" logs the detector output and the position of the chopping mirror as well as various voltages, currents, temperatures, etc. which we use to monitor the telescope. Two versions of the data are recorded. A complete version (≈ 1 G byte/day), which is used in the final analysis, is stored on a 4 G bytes hard drive in the data computer. This drive is contained in a pressurized vessel to prevent damage resulting from operation at high altitude [24]. These drives are swapped out every two to four days. The data are then uploaded onto the computer system in the ground station, and stored on Exabyte tapes. A second compressed version of the radiometry and housekeeping data is bi-phase encoded and sent real time to the ground station.

The "Pointing PC" records the position of the 17-bit absolute digital encoder on the telescope azimuthal bearing, controls and monitors the azimuthal drive motor, records the time from a GPS receiver, and interprets commands sent remotely from the ground station. A CCD camera and Matrox digital image processing board can track stars during calibration and pointing verification procedures. The command status and all other information on the pointing PC is passed to the data PC for logging. The Pointing PC can also reboot the Data PC, an operation we sometimes found necessary.

Two radio links allow us to communicate with the telescope from the ground station. A high frequency link at 1.4 GHz (bandwidth of 100 kHz) with a 2 W transmitter links the data computer with a ground station PC providing the bi-phase data. A marine radio operating at 460.5 MHz communicates via a packet modem with the pointing computer, providing commanding.

The ground station computers receive and store the data, archive the data to tape, and run the commanding, display, and alarm software. From the ground station, the telescope can be slewed in azimuth, chopper parameters can be adjusted, and the cooling power (to stabilize the temperature of the warm electronics) can be increased or decreased. Most major systems can be turned on and off remotely.

7. OBSERVATIONS

While both QMAP and TOCO were designed to measure the anisotropy, their approaches were completely different. QMAP was designed to make a true map of the sky. The data from the time stream were pixelized on the sky and the analysis was done on the sky map. In the first flight of QMAP, the chopper swept horizontally at 4.7 Hz and the gondola wobbled in azimuth with a period of 100 s about a meridian containing the North Celestial Pole. This gondola motion, combined with the rotation of the Earth, produced a highly interlocking scan pattern that allowed for the clean separation of instrumental effects from the celestial signal (de Oliveira-Costa *et al.* 1998).

The TOCO scan was designed to measure the angular power spectrum[25]. The telescope optical axis is fixed in azimuth and elevation, as indicated in Tables 1 & 7, and

[23] One half of an Analog Devices AD1878

[24] When not enclosed in a pressurized and dust-free container, most hard drives, especially high capacity ones, were found to fail on a timescale of a day.

[25] We decided against observing on both sides of the South Celestial Pole (which would have produced interlocking scans thereby facilitated map production) to maximize the stability of the instrument and to minimize the complexities of the analysis.

TABLE 7
TELESCOPE AND CHOPPER MOTION

Parameter	QMAP96a	QMAP96b	TOCO97	TOCO98
Chopper frequency, f_c (Hz)	4.7	4.6	4.6	3.7
Chopper amplitude in azimuth, ϕ_c(max) (deg)	±10	±2.5	±2.96	±2.02
Elevation at center of chop, θ_{el} (deg)	40.7	40.1	40.5	40.63
Azimuth of center of chop [a], θ_{az} (deg)	scanned	scanned	204.9	207.47
Amplitude of wobble (s)	100	50	none	none
Amplitude of wobble in azimuth (deg)	$\pm5°$	$\pm1°.5$	none	none

[a]This is the physical motion in a horizontal plane. The amplitude on the sky is $2\phi_c \cos\theta_{el}$.

the chopper sweeps the beam across the sky. The beams cover an annulus around the SCP as shown in Figure 8.

The TOCO observing site is located at an altitude of 5200 m on Cerro Toco in the Northern Atacama desert in Chile near the borders of Argentina and Bolivia. The latitude is $22°.95$ South and the longitude is $67°.775$ West. A building for an abandoned sulpher mine blocks the occasional 60 kt winds. The Atacama is one of the highest, driest deserts in the world and is therefore a good place for millimeter and centimeter wave observations. We find that the weather is good enough for D-band CMB observations $\approx 50\%$ of calendar time between September and January.

8. CALIBRATION

Calibration uncertainty is the largest source of experimental error for both QMAP and TOCO as it is for many other CMB experiments. In general, calibration is dominated by systematic effects. Multiple independent measurements are required to determine the uncertainty. Short of this, one's knowledge of the experiment is called upon to set the uncertainty and its distribution [26].

A calibration for TOCO involves the following steps: a) position the telescope so that Jupiter either rises or sets through the azimuthally swept beam; b) make a map of the source and find the best fit amplitude, position, and beam profile; c) compute the brightness of Jupiter accounting for its position with respect to Earth; d) correct for slow drifts in calibration, correct for the electronic response of the receivers, and convert Rayleigh-Jeans to thermodynamic temperature. A similar procedure was used for QMAP. In the following, we consider each element of the calibration and its associated uncertainty.

There are two general classes of calibrators, those that fill the beam and point sources. FIRS (Ganga et al. 1993), BOOMERanG, and MAXIMA used the dipole as calibrated by both FIRAS and DMR aboard COBE. The dipole signal corresponds to angular scales larger than, and detection frequencies lower than, those used for CMB data analysis. Thus knowledge of

the electronic transfer function, beam profile, and spatial filtering are necessary for the extrapolation. At the other extreme, point sources are at smaller angular scales and higher post-detection frequencies than those used for CMB analyses. They have the advantage that the calibration and beam profile are measured simultaneously. Still, though, one must account for the electronic transfer function and spatial filtering.

QMAP was calibrated with Cas-A[27] and TOCO was calibrated using Jupiter. As the beam sweeps across the source, the detector output is given by

$$\mathcal{C}V(t) = \frac{1}{2} \int_\nu \int_\Omega \int_{t'} A_e(\nu)g(\nu)S_\nu(\vec{\Omega})P_n(\nu, \vec{x} - \vec{x}'(t')) \times$$
$$I(t - t')d\vec{x}d\nu dt' \quad (13)$$

where V is the voltage out of the detector, A_e is the effective area of the telescope dish, $g(\nu)$ is the passband of the receiver, S_ν is the source surface brightness in units of W/m^2 sr Hz, P_n is the normalized gain of the antenna, $\vec{x}$ is the direction on the sky, and I is the impulse response function of the electronics[28]. Here $\mathcal{C}$ is the calibration constant that relates the source temperature to the measured voltage. We do not explicitly account for sampling in the integral.

Each term in equation 13 has an error associated with it that contributes to the net uncertainty. The effects include: a) σ_S, the intrinsic uncertainty in the brightness temperature of the source at the calibration frequency extrapolated from previous measurements; b) σ_V, the uncertainty in the measured temperature of the source; c) σ_Ω, the uncertainty in the measured solid angle of the beam which includes any beam smearing; d)the uncertainty in the measured receiver bandpass, σ_g, and center frequency, σ_ν; e) σ_{drift}, the uncertainty in the change of the calibration between when it is measured and when it is applied; and f) σ_I, the uncertainty in the frequency response of the instrument. Items (b) and (c) are derived from measurements of the source and are covariant; generally one conservatively treats them as independent errors. Com-

[26] One may, for example, conservatively use the difference between two measurements as the uncertainty (e.g., de Bernardis et al. 2000) even though the formal uncertainty is the difference divided by $\sqrt{2}$. To determine error bars on quantities derived from the data, one marginalizes over the distribution that describes the calibration. Generally the distribution is taken as Gaussian, though one might reach different conclusions if a different distribution in fact described the data.

[27] 3C461, 2321+583IAU(1950), $l = 111°.7$, $b = -2°.1$

[28] A typical frequency dependent loss in the system has a negligible affect on the calibration.

TABLE 8
OBSERVING PARAMETERS

Campaign	Ka1	Ka2	Q1	Q2	Q3	Q4	D1	D2
QMAP96a								
Sample frequency, f_s (Hz)	752	752	752	752	752	752	...	...
Samples per chop, N_s	160	160	160	160	160	160	...	...
Θ_{FWHM} per scan	20	20	30	30	30	30	...	...
Samples per Θ_{FWHM} (F/S)[a,b]	0.78/3.2	.78/3.2	0.56/2.7	0.56/2.7	0.58/2.7	0.58/2.7	...	...
Point Source Sensitivity $\Gamma(\nu_c)(\mu\text{KJy}^{-1})$	128	128	132	132	129	129	...	...
QMAP96b								
Sample frequency, f_s (Hz)	736	736	736	736	736	736	...	...
Samples per chop, N_s	160	160	160	160	160	160	...	...
Θ_{FWHM} per scan	5	5	8	8	8	8	...	...
Samples per Θ_{FWHM} (F/S)	3.1/6.5	3.1/6.5	2.4/5.7	2.4/5.7	2.3/5.6	2.3/5.6	...	...
Point Source Sensitivity $\Gamma(\nu_c)(\mu\text{KJy}^{-1})$	136	136	146	146	120	120	...	...
TOCO97[a]								
Sample frequency, f_s (Hz)	368	368	368	368	368	368	1472	...
Sky detection frequency (Hz)	18-55	18-55	18-64	...	23-64	23-64	...	...
Samples per chop, N_s	80	80	80	80	80	80	320	...
Θ_{FWHM} per scan	6	6	9	9	9	9	30	...
Samples per Θ_{FWHM}[b](F/S)	1.3/3.0	1.3/3.0	1.0/2.6	1.0/2.6	1.0/2.6	1.0/2.6	1.1/5.2	1.7/6.7
Point Source Sensitivity $\Gamma(\nu_c)(\mu\text{KJy}^{-1})$	131	131	128	120	119	118	87.3	49.5
TOCO98[a]								
Sample frequency, f_s (Hz)	296	296	296	296	296	296	1184	1184
Sky detection frequency (Hz)	...	...	...	...	...	...	19-59	19-63
Samples per chop, N_s	80	80	80	80	80	80	320	320
Θ_{FWHM} per scan	4	4	6	6	6	6	20	20
Samples per Θ_{FWHM} (F/S)	1.9/3.6	1.9/3.6	1.5/3.2	1.5/3.2	1.4/3.0	1.4/3.0	1.7/6.7	2.5/8.1
Primary Aperture Efficiency, η_p	0.58	0.58	0.65	0.62	0.56	0.55	0.52	0.24
Chopper Aperture Efficiency, η_p	0.10	0.10	0.11	0.11	0.10	0.10	0.087	0.040
Point Source Sensitivity $\Gamma(\nu_c)(\mu\text{KJy}^{-1})$	121	121	138	131	119	116	117	54.7

[a]F/S refer to the fast and slow parts of the sinusoidal motion near the center and edges of the chop.

[b]The sky is not Nyquist sampled at the center of the chop. This is accounted for in the mapmaking and beam synthesis. The e^{-1} point of the beams, $l_e = \sqrt{16\ln 2}/\theta_{FWHM}$, is $l_e = 212, 273$, and 955 for Ka, Q, and D respectively. The undersampling for QMAP96a is severe and limits the map reconstruction in the current pipeline to $l \approx 180$.
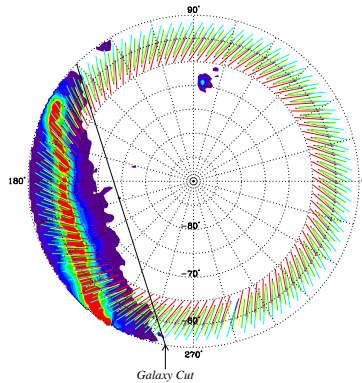

FIG. 8.— Scan pattern for the TOCO98 campaign around the SCP. The scans are shown as straight lines for each feed for 15 minute intervals around the sky. A more detailed picture would show the lines with slight curvature to account for the projection. The center of the chop is at an azimuth of $207°.5$ and an elevation of $40°.6$. The chopper sweeps out $6°.12$ on the sky as it scans in azimuth. This results in a ring around the SCP approximately centered on $\delta = -61°$. The map of the galaxy is from Schlegel *et al.* (1997).

bining these sources, the intrinsic calibration is given by:

$$\left(\frac{\sigma_c}{C}\right)^2 = \left(\frac{\sigma_S}{S}\right)^2 + \left(\frac{\sigma_V}{V}\right)^2 + \left(\frac{\sigma_\Omega}{\Omega}\right)^2 +$$

$$\left(\frac{\sigma_{drift}}{drift}\right)^2 + \left(\frac{\sigma_I}{I}\right)^2 \quad (14)$$

We evaluate these terms in the following and summarize the results in Table 9.

8.1. Calibration Source Brightness Temperatures

The flux from a source is typically given as $f_\nu = \int S_\nu(\theta, \phi)d\Omega$ and is reported in units of Janskies ($1\,\mathrm{Jy} = 10^{-26}\,\mathrm{W/m^2\,Hz}$) as a function of frequency. A power-law model is used to extrapolate the calibration frequencies to the observation frequency, $f_\nu = f_0(\nu/\nu_0))^\beta$. When the source angular size is a significant fraction of the beam or is changing in time, as it is for planets, it is more convenient to use the brightness temperature.

8.1.1. Cas-A Flux for QMAP

Cas-A is unresolved at the QMAP beam size and the correction for its finite size is negligible. From a combination of the data (Baars *et al.* 1977; Chini *et al.* 1984; Mezger 1986), we find $\log(S_\nu/\mathrm{Jy}) = (5.713 \pm 0.023) - (0.759 \pm 0.006)\log(\nu/\mathrm{MHz})$ at epoch 1980 (Herbig *et al.* 1998). At 31.3 GHz, the mean frequency of the QMAP Ka bands, the flux corresponds to 199.9 Jy. Baars *et al.* (1977) give the percentage annual decrease as $\delta S_\nu/S_\nu = 0.97(\pm 0.04) - 0.3(\pm 0.04)\log(\nu/\mathrm{GHz})$ and so this value is reduced to 183 Jy for epoch 1997. When one takes into account all of the above errors, including σ_ν, the uncertainty is $(\sigma_S/S) = 8.7\%$ for both Ka and Q bands.

After the QMAP data release, Mason *et al.* (2000) reported $S_{cas,1998} = 194 \pm 4.7$ Jy at 32 GHz which we convert to 195 Jy for epoch 1997. This measurement, which is very close to our frequency, greatly reduces the uncertainty associated with the interpolation and secular decrease. When the errors in the central frequency are included (Table 1), the uncertainty is $(\sigma_S/S) = 2.7\%$. For Q band, the flux is 159 ± 4.8 Jy. The slightly larger error is from the extrapolation from 32 to 41 GHz. The result is an increase in the temperature scale of the QMAP data by 6.6% and reduction in the calibration uncertainty, σ_S.

8.1.2. Jupiter Temperature for TOCO

The brightness temperature of Jupiter is measured by Ulich (1981), Griffin *et al.* (1986), Ulich and Mason *et al.* (2000), and is taken to be 152, 160, and 170 K in Ka, Q, and D band respectively with an intrinsic calibration error of $\sigma_S/S = 5\%$. As the temperature is a weak function of frequency across our bands, the uncertainties resulting from σ_ν and σ_F are negligible. The Jupiter calibration temperature is obtained by scaling the brightness temperature by the ratio of the solid angle of Jupiter (determined from ephemerides) to the measured solid angle of the beam. A typical measured temperature of Jupiter is 15 mK, 30 mK, and 350 mK in Ka through D1 bands respectively.

Finally, one applies a correction to convert small changes in antenna temperature to small changes in thermodynamic CMB temperature. We use:

$$\eta = \left(\frac{\partial T_{\mathrm{ant}}}{\partial T_{CMB}}\right) = \frac{x^2 e^x}{(e^x - 1)^2} \quad (15)$$

where $x = h\nu/kT_{CMB}$. For the TOCO98 D-band data, the data are multiplied by η^{-1}, or 1.66 for D1 and D2 to convert from data calibrated on Jupiter's brightness temperature to thermodynamic units referenced to the CMB. For the Ka and Q band data we multiply by 1.02 and 1.05 respectively. The error in these measurements depends on the knowledge of the band centroids and introduces $\leq 1\%$ uncertainty.

8.2. Measured Beam Solid Angle and Temperature

To convert the measured fluxes to a temperature, the beam solid angle must be known. Table 5 gives the beam determination for all campaigns along with the results of a computer model. For QMAP, the solid angle was determined from one in-flight mapping of Cas-A (Herbig *et al.* 1998). The statistical error on the fit varied between 1% and 3% depending on the flight and band. As the beam fitting includes modeling of the instrumental offsets, there is additional systematic error resulting in a net uncertainty of $\sigma_\Omega/\Omega = 5\%$. For TOCO, the beam solid angles were determined from a global fit to the Jupiter calibrations made during good weather. This was done separately for both campaigns. In total, Jupiter was mapped over 70 times. All results from the four campaigns are consistent with our models. From all of our measurements of the beams, we conclude that the error on the solid angle for Ka and Q bands is 5%, for D1 it is 5%, and for D2 it is 5.5%. These values are dominated by systematic errors.

It is often convenient to parameterize the beams with a two dimensional Gaussian profile. For Ka and Q bands, this introduces a negligible error. We tested for this in TOCO97 (Torbet *et al.* 1999) analysis where we used the measured Ka and Q-beam profiles in place of the parameterized profiles and found $< 1\%$ difference in the final results. The D-band channels are less well approximated by Gaussian profiles and thus one must use the measured profile for accurate results as was done in Miller *et al.* (1999).

For each calibration, a seven parameter model is fit to the data. We find the position of the source, the best 2-D Gaussian parameterization including orientation, the amplitude, and an offset. For QMAP, the 1-2% statistical error on the amplitude is dominated by a 3% systematic uncertainty in the algorithm to extract the amplitude. In the TOCO experiment, the standard deviation of the fitted amplitude is 4-10% for all the HEMT channels in both seasons. The variance is a result of atmospheric fluctuations and finite HEMT sensitivity and thus averages down as the square root of ≈ 20 independent high quality maps in each season to a value of 2%. There is a small additional uncertainty due to the fact that not all fitting algorithms give the same results. The net result is to increase the uncertainty in the amplitude to $\sigma_V/V = 3\%$.

8.3. Calibration drift

The physical temperature of the TOCO instrument can vary by 50 K in a day. Even though all critical components are thermally regulated, there are temperature changes

that lead to changes in gain. Jupiter was observed, on average, within two hours of the beginning of the CMB observing time. Changes in system gain on time scales shorter than 24 hours were monitored with an internal calibration signal ("cal pulse") with an effective temperature of ≈ 1 K in all bands. This pulse was turned on 40 msec twice every 200 seconds. The amplitude of the pulse was regressed with the body temperatures of the noise sources, warm electronics temperatures, and cryogenic temperatures in all bands. The fit coefficients are consistent with laboratory measurements and show that the pulse amplitude is constant but that the system gain is a function of the microwave amplifier temperatures.

For TOCO, a typical long term (50 days) variation is 15% in Ka band, 5% in Q band, and 20% in D-band. The cal pulse amplitudes follow the general trends in the Jupiter calibrations in all bands. From the cal pulses and the Jupiter observations, we derive a calibration drift model which we apply to the data. In D-band, atmospheric fluctuations made use of the cal pulses to correct drifts over periods of less than six hours problematic. The uncertainty in the model is estimated to be 5%.

A similar approach was taken with QMAP though the cal pulses were clearer and so the uncertainty in correcting for the 5% drift is negligible.

8.4. Electronic passband

Observing a point source is similar to exciting the electronics with a pulse. Consequently there are frequency components up to $f \approx 4[\phi_c \cos(\theta_{el})\theta_{FWHM}]f_c$ (Table 7) of the post-detection electronics. The CMB signal is at comparatively lower frequencies. We model the full electronic response of the system, including sampling, and find that the CMB data should be reduced by 1.7% in D-band, 1.5% in Q-band, and 1% in Ka-band for TOCO and 1.5% for QMAP over what one would get without the correction. We estimate the uncertainty in this to be 1% for TOCO and 5% for QMAP. These shifts were not reported in the original papers as they were much smaller than the uncertainty, though we include them here.

From Table 7, one sees that we are slightly undersampled during the fastest part of the chop (where the least amount of time is spent). To check for a possible systematic effect in TOCO associated with this, calibrations were done with the source at the center of the chop and off to one side and with different chopper amplitudes. The results of these tests are statistically consistent with the nominal calibrations. For TOCO, the CMB anisotropy results are insensitive to the slight undersampling because the CMB detection frequency is far below the sample frequency–due to the beam synthesis–and because in the beam synthesis we simulate the sky scan.

For the first flight of QMAP the undersampling is more drastic and was not included in detail in the mapmaking. Thus, the QMAP data should only be considered valid up to $l = 180$[29]. For both flights, the calibration data were processed in a manner similar to the mapmaking and so beam smearing effects were accounted for in an average sense.

The phase response of the full instrument as a function of frequency was measured in the lab and determined from observations of the Galaxy and Jupiter. We find that the phase is linear over the range of frequencies applicable to both CMB and point source observations.

8.5. Combining the calibrations between bands and systematic shifts from previous results.

Both QMAP and TOCO have multiple detectors, the measurements of which are combined into one angular spectrum. The net calibration uncertainty is a combination of terms that are completely correlated between channels, such as σ_S, σ_Ω, σ_{drift}, & σ_I, and terms that are uncorrelated, such as σ_V and σ_η. When the data are combined the last two terms become negligible. The uncertainties are 8% for D1+D2, for the TOCO HEMTs, and for the combination of the D1+D2+HEMTs. For QMAP the net uncertainty is 7.6%. In the regions where the QMAP and TOCO angular spectra overlap, only σ_S and σ_Ω are correlated and the combined uncertainty is 6.4%.

These uncertainties are slightly different than those previously quoted for these experiments and are the result of a complete reassessment of the calibration errors. To correct the previously published results, the QMAP data should be multiplied by 1.051, The TOCO D-band data (Miller *et al.* 1999) should be multiplied by 0.983, and the TOCO HEMT data (Torbet *et al.* 1999) by 0.99.

9. OBSERVING THE ANISOTROPY

The anisotropy is a two dimensional random field in temperature. The goal of CMB anisotropy experiments is to measure the characteristics of that field. The three methods in use are direct mapping, time-domain beam synthesis, and interferometry. For a small number of detectors, direct mapping makes the most efficient use of them, beam synthesis is the next most efficient, and interferometry is the least efficient, as we discuss in Section 10. The best strategy to use, though, depends as much on the control of potential systematic errors as on raw sensitivity.

The QMAP experiment was designed to make a direct map. By this we mean that the time ordered data are assigned a sky pixel number as they come out of the detector. Slow drifts in the detector output may be removed from the map using a variety of methods (Cottingham 1987; de Oliveira-Costa *et al.* 1998; Hivon *et al* 2001). For all methods, though, a heavily interlocking scan strategy is required for robust results. QMAP produced multiple $\approx 0°.8$ resolution maps of the CMB from two flights. These maps were found to be consistent with each other and with the Saskatoon maps (Xu *et al.* 2000). In other words, two entirely separate experiments measured the same temperature variations in the sky in overlapping regions. The other mapping experiments to do this are COBE/DMR (Smoot *et al.* 1992) with FIRS (Ganga *et al.* 1993), and COBE/FIRAS with COBE/DMR (Fixsen *et al.* 1997). A wide range of systematic checks have been applied to QMAP and it passes them all.

The TOCO experiment used time-domain beam synthesis[30]. To our knowledge, the method was first employed in Netterfield *et al.* (1995). Since the Saskatoon experiment,

---

[29] Neither the undersampling nor the calibration shift were accounted for in Xu *et al.* (2001) and Wang *et al.* (2001).

[30] Atmospheric fluctuations preclude direct mapping from the ground.

Channel	σ_S (%)	σ_Ω (%)	σ_V (%)	σ_{drift} (%)	σ_η (%)	σ_I (%)	σ_C (%)
D1	5	5.5	3	4	1	1	9.1
D2	5	5	3	4	1	1	8.8
TOCO HEMTs	5	5	3	4	$\cdots$	1	8.7
QMAP HEMTs	2.7	5	3	$\cdots$	$\cdots$	5	8.1

The intrinsic Jupiter calibration uncertainty is given by σ_S (Section 8.1), σ_Ω is the uncertainty in measured solid angle (Section 8.2), σ_V is the uncertainty in measured Jupiter brightness temperature (Section 8.2), and σ_{drift} (section 8.3) is the uncertainty due to the calibration drift between observations, σ_η refers to the Rayleigh-Jeans to thermodynamic conversion due to the uncertainty in the centroid, and σ_I is the uncertainty on the electronic bandpass correction. These calibration errors are in temperature.

we have refined the technique, applied it to a multifeed system, and incorporated numerous cross checks and systematic checks of the robustness of the solution. Most of the remainder of this paper is devoted to describing those checks.

10. TIME DOMAIN BEAM SYNTHESIS

As with all ground-based CMB experiments, the effects of atmospheric fluctuations must be strongly suppressed. TOCO uses the chopping flat to scan the beam across the sky in a sinusoidal pattern (Section 4.2). In a postdetection analysis, the time ordered data are multiplied by synthesis vectors, $SV_{n,i}$, that have half the period of the chopper cycle. Thus, the data with the chopper moving in one direction is coadded with the data with the chopper moving in the other direction. We form

$$t_n = \sum_{i=1}^{N_c} SV_{n,i} d_i \qquad (16)$$

where d_i is the vector containing the raw data from a full chop cycle, n is the index or "harmonic" of the synthesized beam, and N_c is the number of samples in a chop cycle.

There is no set prescription for $SV_{n,i}$. The best choice depends on the scan pattern (e.g., sinusoidal or triangular), the desired degree of orthogonality between synthesized beams, the shape of the resulting window function, and the orthogonality to any potential offset. For instance, one may pick $SV_{n,i}$ so that t_n is insensitive to the secant dependence of the atmospheric gradient. For the sinusoidal scan patterns, we find a useful set is given by

$$SV_{n,i} \propto \cos(\pi(n-1)(1-\sin(2\pi(i-1/2)/N))/2), \quad i = 1, ...N_c \qquad (17)$$

though ultimately we tune the $SV_{n,i}$. The synthesis vectors are effectively apodized sine functions each of which is designed to produce a different effective antenna pattern, and thus probe a different angular scale.

The phase of the electronic signal with respect to the position of the beam on the sky is determined by forming the quadrature signal (data from the first half of chopper sweep minus data from the second half resulting in minimal sensitivity to celestial signals) as a function of phase for each harmonic. Then the phase that nulls the galactic signal over twenty-five of the best observing days is found. There is a small harmonic dependent component to the best fit phase that is well modeled with a linear

fit. The phase shift is incorporated into equation 17 for all analyses. The galaxy-null determined phases agree with the phases determined from Jupiter observations, derived with completely independent code. In addition, the entire data analysis is redone after setting the phase ahead and behind the best fit by twice the error derived in the fit. No changes in the final results are seen.

The resulting effective antenna sensitivity patterns, or synthesized beams $H(\mathbf{x})$, are given by

$$H(\mathbf{x}) = \left\langle \sum_i SV_i G(\mathbf{x} - \mathbf{X_i}) \right\rangle_{\text{RA bin}} \qquad (18)$$

where the center of the main beam is located on the sky at position $\mathbf{X_i}$, SV_i is the synthesis vector, and

$$G(x,y) = \frac{1}{2\pi\sigma_x\sigma_y} \exp\left(-\frac{x^2}{2\sigma_x^2} - \frac{y^2}{2\sigma_y^2} \right) \qquad (19)$$

is the main beam pattern of the telescope pointed at the center of the chop. Here x measures the position in the azimuthal direction, y changes with elevation, and the beamwidth of the telescope is $\sigma = \theta_{\text{FWHM}}/\sqrt{8\ln 2}$. Beam smearing due to the finite size of the sky bins is incorporated into equation 18. As tests, the A/D sampling and the change in the effective horizontal beam width as a function of chopper speed are included in equation 19. These effects are negligible. As noted earlier, equation 19 was replaced with the true beam profile for D band. This was not necessary for the other bands. The synthesized beams are then normalized, by adjusting the amplitude of $SV_{n,i}$, so that:

$$\int |H(\mathbf{x})| d\mathbf{x} = 2 \qquad (20)$$

In summary, the synthesis vectors and beam synthesis incorporate all known aspects of the motion of the beam on the sky.

Data are binned according to right ascension at the center of the chopper sweep into 768 "fundamental bins" around the complete circle shown in Figure 8. The fundamental bins are subgrouped into N_{RA} right ascension bins where N_{RA} depends on the harmonic. Thus, the average in equation 18 depends on harmonic. To avoid statistical bias, it is important that the mean, sample variance, and error on the mean in each of the N_{RA} bins is computed for *all* the data that land in a bin in a given night.

For example, for the 1998 4-pt[31], Q-band beam, there are $N_{RA} = 20$ bins around the circle and so in one night, $\approx 1.7 \times 10^4$ values of t_4 (equation 16) are averaged together for each bin. At low l, the variance in any RA bin is larger than that expected from detector noise alone due to atmospheric fluctuations. For integrations longer than roughly 3 minutes, the noise is stationary for the cuts described below. Finally, the results from individual nights are averaged.

The harmonics are analyzed individually at low l or in groups at higher l. Data from different detectors are also combined. The full theory covariance matrix, C_T, is computed for each harmonic or combination (Bond 1996) along with the Knox filter (Knox 1999) and effective spherical harmonic index, l_e, of the observations. The noise covariance matrix, C_N, is computed from the data. Other than detector noise, which is uncorrelated between bands, the dominant contribution is the atmosphere. Unlike Saskatoon, the frequency bands are not subdivided and there is no East-West chopping.

For each group of harmonics, we find the likelihood as a function of the band power, δT_l^2, according to[32]:

$$L(\delta T_l^2) = \frac{1.}{2\pi^{N/2}|\mathbf{M}|^{1/2}} \exp(-t^T \mathbf{M}^{-1} t/2), \qquad (21)$$

where $\mathbf{M} = C_T(\delta T_l^2) + C_N$. All the analysis is done as a function of δT_l^2, though we report δT_l because it gives a direct measure of signal-to-noise as the detector output is proportional to temperature.

It is sometimes convenient to estimate the signal-to-noise for a single measurement for a single harmonic. This can then be generalized to a set of N independent measurements (Knox 1995). The measured *rms* amplitude of the sky fluctuations is given by $\Delta = \delta T_l \sqrt{I(W)}$ where $I(W) = \sum_l (W_l/l)$, with W_l the window function, encodes the efficacy of the synthesized beam. The noise of any measurement is given by $\kappa_n \tilde{T}/\tau_{obs}^{1/2}$ where [33] $\kappa_n = \left[N_c \sum_{i=1}^{N_c} SV_{n,i}^2 \right]^{1/2}$, τ_{obs} is the time spent observing a point, and $\tilde{T}$ is given by equation 2. From fits to the computed $I(W)$, we find $\sqrt{I(W)} \approx 2.6/n^{0.75} \approx 6/\sigma_b^{0.25}l_e^{0.75}$ where n denotes the n-pt function, σ_b is the Gaussian width of the beam, and l_e is the associated effective spherical harmonic index. The signal-to-noise for a particular measurement is then

$$S/N = \frac{\delta T_l \sqrt{I(W)} \tau_{obs}^{1/2}}{\kappa_n \tilde{T}} \approx \frac{0.7}{\sigma_b^{0.5}l_e^{0.8}} \frac{\delta T_l \tau_{obs}^{1/2}}{\tilde{T}} \qquad (22)$$

We may interpret this result as saying that for a fixed sensitivity, $\tilde{T}$, and a flat angular spectrum, δT_l, beam synthesis reduces the effective temperature of the sky by $\gamma^{TDBS} = 0.7/\sigma_b^{0.5}l_e^{0.8}$. This form fits Ka-band through D-band data to 30% accuracy for TOCO [34].

It is worth contrasting beam synthesis in interferometry with time domain beam synthesis. In interferometry, each baseline yields one synthesized beam en-

veloped by the primary beam pattern of a single element. A similar expression to equation 22 obtains for interferometers with Gaussian main beams of width σ_b^{Int} (Hobson *et al.* 1995; White *et al.* 1998). We find

$$S/N = \frac{\sqrt{2}}{\sigma_b^{Int}l_0} \frac{\delta T_l \tau_{obs}^{1/2}}{\tilde{T}} = \gamma^{Int} \frac{\delta T_l \tau_{obs}^{1/2}}{\tilde{T}} \qquad (23)$$

where $l_0 = 2\pi u_0$ is determined by the separation of the two antennae. For the 5-pt Q-band synthesized beam, $\theta_{FWHM} = 0°.7$ ($\sigma_b = 0.0052$) and $l_e = 87$. Similar coverage in l-space would be obtained with an interferometer with $\theta_{FWHM} = 4°.86$ ($\sigma_b^{Int} = 0.036$) and $l_0 = 87$. From these, $\gamma^{TDBS} = 0.27$ and $\gamma^{Int} = 0.45$. To the level of accuracy of the fitting functions, these are equivalent.

The sensitivity advantage of time domain beam synthesis is that multiple n-pt functions are measured simultaneously with a single detector. In the parlance of Fourier transform spectroscopy, there is a multiplex or "Felgate" advantage over an interferometer with just a few antennae. However, as the number of interferometer baselines scales as $n_a(n_a - 1)/2$, where n_a is the number of antennae, large interferometers achieve high sensitivity (Padin *et al.* 2000; Pryke *et al.* 2001). For the ideal mapping experiment, with minimal baseline subtraction, the advantage over both interferometry and time domain beam synthesis is that in a fixed amount of time more spatial modes can be measured.

11. DATA SELECTION

Most of the analysis effort goes into data selection and testing to make sure that the selection does not bias the final result. The largest cuts remove data contaminated by the galaxy, by the atmosphere, and by unstable offsets. Partial descriptions of the cuts are given in Miller *et al.* (1999) and Torbet *et al.* (1999). In this section we describe the cuts for the TOCO98 D-band data and the consistency checks as they are indicative of the process for all channels. A summary of the cuts is given in Table 10.

11.1. Cuts to the time line

The initial cuts are made to the raw time-ordered data in order to excise extreme events, such as a nearby object entering the beam or very bad weather. Data are examined in 6.5 second averages (24 chop averages with $f_c = 3.7$ Hz). The internal calibration pulses are removed and a rough cut is made at a nominal *rms* level based on the long term observing characteristics. This cut removes $\approx 50\%$ of the data.

The next set of *rms* cuts is made to the synthesized data. In general, the higher harmonics are less sensitive to atmosphere and therefore require less severe cuts. The data are binned into fifteen minute averages and, for each harmonic on each day, the minimum value of the average *rms* is selected as the baseline. For D1, all data within 25% of the minimum are accepted for harmonics 8-21. For harmonics 5-7 everything within 20% is accepted. For the

---

[31] Following the notation in Netterfield *et al.* (1997), we call a synthesized beam with n lobes an n-pt beam (see Figure 5).

[32] In this paper, we report the band power following Bond as opposed to Netterfield. The difference is $2(l + 1)/(2l + 1) \approx 0.2$ % at $l = 200$

[33] For the classic single difference, $\kappa = \sqrt{2[1^2 + (-1)^2]} = 2$.

[34] Other functional forms work as well. This is presented to aid in estimating the S/N. For SK, which used different criteria to synthesize the beams, $\gamma^{TDBS} = 3.6/\sigma_b^{0.5}l_e$, roughly a factor of two higher at low l. However, the window functions were less well localized.

case of D2, harmonics 8-17 are cut at 30%, and 5-7 are cut at 20%. Harmonics ≤ 4 are rejected entirely as they are corrupted by atmospheric fluctuations.

We analyze 28 nights for D1 and 23 for D2. (The number is higher for D1 due to high offsets in D2 on several nights leading to the decision to exclude these data from the analysis.) In order to prevent signal contamination from times of large atmospheric fluctuations, the previous and subsequent fifteen minute segments are eliminated from each segment cut by the above criteria. The effect of this cut is to keep 5-10 hour blocks of continuous good data in any day and to eliminate transitions into periods of poor atmospheric stability. On a typical day that passes the initial *rms* cut, an additional 40% of the synthesized data is removed due to atmospheric fluctuations. The net result is that 26% of the data are kept.

As discussed above, data are placed into 768 bins in right ascension with RA=0° corresponding to the first bin. All data falling between bins 288 and 555 are cut in order to eliminate observations of the Galaxy from the CMB analysis. This is equivalent to cutting all data with $135° < RA < 260°$ centered at $\delta = -60°$. By observing at an azimuth of 208°, the galaxy cut occurs during the day, when the data are not generally useful for CMB observations at 144 GHz because of the atmosphere. The Galactic cut overlaps well with the atmospheric cut. On a day during which there are minimal atmospheric fluctuations, we end up cutting only 35% of the data.

When the *rms* chopper position over a single chop deviates by more than 0°.015 from the average position, the data are cut. This includes times when the chopper is intentionally shut off due to testing and maintenance as well as time during high winds. This cut eliminates $\approx 3\%$ of the data.

The absolute timing is done through the Global Positioning System (GPS). Data are eliminated during GPS drop-outs. There was also an error in the first frame of each logical file which made the GPS read out incorrectly for that frame. The first file in each set is therefore rejected ($\approx 5\%$ of the data). The files were generally started directly following a calibration or during the day when we were at the telescope, thus the percentage of these data which would otherwise be retained for CMB analysis is small.

11.2. *Cuts to the binned data*

The goal of the cuts to the binned data is to ensure that only long periods of uninterrupted data are included in the final analysis. We cut away the low density regions by removing any fundamental bin with fewer than fifteen of the adjacent bins filled. This is done twice to ensure that stragglers are removed. Finally, the entire file (approximately one day) is removed if there are fewer than 100 usable bins (approximately three hours of uninterrupted clean data). More than 90% of the days analyzed for CMB anisotropy have continuous 5-10 hour blocks of data.

11.3. *Offset Removal*

An offset is the value of a given harmonic when the signal on the sky is zero. Equation 16 gives the expression for an element of synthesized data. Each element in the final data file is the average value over the RA bin,

$$t_n^{bin} = \frac{1}{N_{cib}} \sum_{j=1}^{N_{cib}} t_{n,j}, \qquad (24)$$

where $t_{n,j}$ is the result from each chop cycle and N_{cib} is the number of chopper cycles in a RA bin. Thus, on a given night, each RA bin has a single value of t^{bin} for each harmonic. These values are examined as a function of RA bin and both a slope and a mean are removed from each harmonic on each night before the nights are combined in order to reduce the potential effect of variations in the offset over long timescales. The slope subtraction has little effect on the final result; its removal is prudent though not essential.

Because the best data do not exactly overlap each night, a potential bias occurs when the mean and slope are subtracted over different regions of sky. Typical offsets for the TOCO98 D-band data are $\approx 150 \pm 75 \, \mu$K in absolute value and drift over a timescale of days. When each full night of data of one harmonic is coadded and analyzed as a function of night throughout the campaign, χ^2/ν for deviation from a flat line is between one and four. The high-l offsets are generally more stable. Because we keep only large sections of contiguous data and because the offset is stable, the effect of slightly different sky coverage per evening is negligible. In the analysis, we approximate the slope and offset removal as removing a single mean and slope from the entire data set as discussed below.

The chopper-position dependent offsets (Figure 6) discussed in Section 5 are effectively filtered by the beam synthesis. We check this by applying the synthesis vectors to the average chopper-synchronous signal by setting $d_i = O_i$ in equation 16. We then examine the variation in the resulting synthesized offset as a function of harmonic and observing night. We find that the standard deviation of the resulting O_n is $< 20\mu$K for the harmonics used in the analysis. Because the offsets are subtracted, this variation does not affect the final result.

11.4. *Ergodicity of noise*

Well defined noise properties are essential for the analysis of CMB data. After the offset subtraction and data cuts, we grid the t_n for each harmonic with pixel number vs. night of observations. We find that the average error bar is independent of night and pixel number. For a given pixel, we also check that the variation in the mean value from night to night is consistent with the average of the variances separately determined each night.

In the high signal-to-noise channels, δT_l^2 can be found by forming:

$$\delta T_l^2 = (\Delta_{tot}^2 - \Delta_{inst}^2)/I(W) \qquad (25)$$

where Δ_{tot}^2 is the total variance of the data for one harmonic and Δ_{inst}^2 is the average variance due to instrument noise. For $l \leq 200$, the results from this calculation are within 10% of the results for the full likelihood analysis (Torbet *et al.* 1999). At $l < 150$ the noise is potentially the most problematic because the offsets are generally larger and the contribution from the atmosphere is larger than for the higher l data. That a simple method based on average noise properties gives the same answer (within 1σ) as the full likelihood analysis, with its detailed attention to correlations and drift subtraction, gives us

<center>Table 10</center>
<center>Cuts for TOCO98 D-band data</center>

Data cuts for the season	
Total number of days analyzed[a]	54 days
Number of days used (D1)	28 days (52%)
Number of days used (D2)	23 days (47%)
Percentage of data kept on good day	53%
Net percentage kept[b]	26%
Data cuts for a typical good day	Data Removed
Galaxy	32%
rms (overlaps with Galaxy cut)	24%
Chopper	3%
Pointing	1%
GPS (overlaps with *rms* and Galaxy cut)	5%
Net cut before beam synthesis	41%
Net cut after beam synthesis	45%
Net cut to the binned data[c]	47%

[a]This is the number of consecutive days on which the SIS system operated. After 54 days, the refrigerator cold head malfunctioned and heated to the point where the SISs were unusable.

[b]This is the net observing efficiency for data of sufficient quality for CMB analysis.

[c]This corresponds to 53% of data kept on a good day.

confidence that the noise estimates are robust and stable. There is nothing in the instrument or sky of which we are aware that changes at the temporal frequencies and spatial scales associated with $l > 200$. Although the signal to noise is lower for large n-pt beams, the data are stable and insensitive to cuts.

12. LIKELIHOOD ANALYSIS AND TESTS OF DATA SELECTION

We find the most likely value of δT^2 as a function of angular scale with a Bayesian likelihood analysis of the cleaned data. The method follows the analysis of the Saskatoon data though the correlation matrices are considerably simpler due to the observing strategy and the focal plane array. One feature of the likelihood analysis is that that channels and harmonics can be combined in a precise and unambiguous way to increase the signal-to-noise. An added benefit of the combined bands is that correlation between combined bands is reduced over that for a single harmonic. The likelihoods for the HEMT data and SIS data are shown in Figure 9.

We test that data selection eliminates the atmospheric and instrumental contaminants without biasing the result by performing a set of internal consistency tests or null tests. Data are multiplied by several different sets of synthesis vectors that have no sensitivity to the sky signal and the analysis is carried out in the same way as for the data which have been multiplied by the sky-sensitive synthesis vectors. We determine that the data have been properly selected when the set of null tests fails to show a signal for individual synthesized beams. The data selection is therefore blind to the signal on the sky, minimizing potential bias introduced by expectations.

The four null tests probe different time scales. The quadrature signal, the difference in signal between the first and second half of the chop, is sensitive to variations at 2 Hz. For the fast and slow dither, we look at the difference between subsequent 0.5 second and 10 second averages respectively. We also examine the difference night to night and between the first and second half of the campaign. In the TOCO98 analysis of individual harmonics for each channel, there was one "failure" ($> 2\sigma$ deviation from a null signal) out of 120 tests, well within expectations. The results of some of the null tests for the full bands are shown in Figure 9.

12.1. *Effects of selection criteria on the data*

Following the selection of the best cuts, we relax the selection criteria or methods in four ways. For each test, we perform the full likelihood analysis. We emphasize that the nominal cut is based on the null tests, not the data. When the criteria are relaxed, the null tests either show signs of contamination, when the likelihoods change, or are unaffected, when the likelihoods do not change. In the following we focus on the D-band data, though similar tests were performed on the HEMT data.

Test 1: The minimum number of filled bins on a given day is increased from 100 (≈ 3 hours) to 250 (≈ 8 hours) and all days not common to both D1 and D2 are rejected from the analysis. The result is a decrease in the significance of the detections (due to permitting less data in the final analysis) but a change of less than 1σ for the two low-l points and less than $\sigma/2$ for the three high l points.

Test 2: The nominal calibration model is determined from fits to Jupiter and the internal calibration pulses. Instead, we perform the analysis simply using the calibration value of the closest Jupiter calibration. The result is a change of less than $\sigma/2$, primarily due to a different calibration.
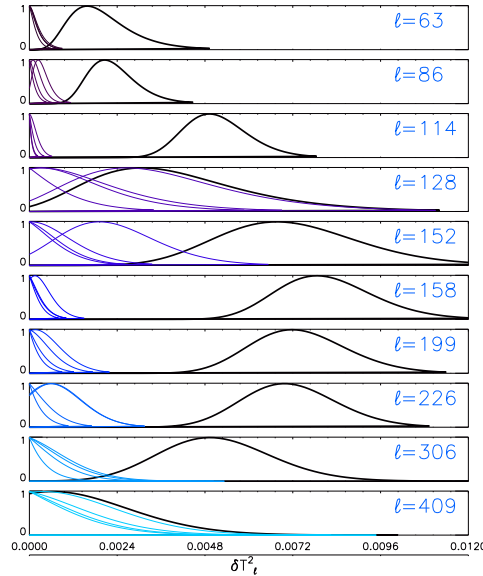
Test 3: We make the harmonic dependent cut to the

FIG. 9.— Likelihood plots for the TOCO data. All likelihoods are normalized to unity at the maximum. The x-axis is δT_l^2 in units of $(mK)^2$. The value on the right of each panel corresponds to the effective l for each Knox filter. The thick contours are for the data. The thinner lines are the likelihoods for the null tests: quadrature, fast dither, slow dither, and first half minus second half signals. The $l = 128$ D-band channel is possibly contaminated by the atmosphere, though the distribution of the null tests is consistent with noise. The null test that is close to the signal is from the slow dither and of all the null tests is the one most different from zero. Such $\approx 1.5\sigma$ deviations are not statistically unexpected. This figure clearly shows the rise and fall of a peak in the CMB angular spectrum. Furthermore, it shows that the null tests are consistent with zero signal. The D-band data are at $l = 128, 152, 226, 306, \& 409$.

synthesized data more stringent. Instead of cutting 45% for a typical good day as shown in Table 10, 65% is cut. The more stringent cut is most pronounced in the lower harmonics because they are most affected by atmospheric contamination. The cut results in upper limits for the $l = 128$ and $l = 158$ points, consistent with the decreased amount of data. Above the 7-pt, the amount of data cut and the resulting likelihoods change very little. We also perform this test by eliminating just 50% (as opposed to 45%) with similar results.

Test 4: We apply only the initial cut to the raw data and so on a typical good day, 41% of the data are kept (before the Galaxy cut). This has the effect of introducing some atmospheric contamination. The result is that the $l = 128$ and $l = 158$ points show an increase in signal of 0.8σ and 1.3σ respectively while the data points corresponding to the highest three groups of harmonics show no significant change.

We have emphasized the TOCO98 D-band data because the points at $l = 128$ and $l = 152$ are more sensitive to the cuts than all the other data. This is due to the large atmospheric opacity at 144 GHz and large angular scales. The nominal cut corresponds to the best null tests and corresponds roughly to the sections of raw data one would select by eye. The D-band data for $l > 200$ are insensitive to the cuts as are all of the HEMT data.

12.2. Correlations

The off-diagonal terms in the noise correlation matrix, C_N, are small. The atmospheric correlation coefficients between channels (Q and Ka band) for TOCO97 and between D1 and D2 for TOCO98 are of order 0.05. We examine the autocorrelation function of the data for individual harmonics and find negligible correlations between

RA bins (due to atmospheric fluctuations). The largest off-diagonal terms in $\mathbf{M}$ are < 0.4 and are in C_T. As part of our checks, we ensure that the likelihood is stable to changes of $\approx 30\%$ the values of the off-diagonal terms.

13. TESTS FOR SYSTEMATIC EFFECTS

There are potential sources of systematic error that would not be revealed by the tests described above. These sources of error, along with their maximum contribution to the data, are summarized in Table 11 and described below. Again, we focus on the D-band data. We note that no effect significantly affects the final results and in particular no effect can produce the decrease in power that is observed between $l \approx 200$ and $l \approx 400$.

The systematic effects involve either beam smearing (Sections 13.1 - 13.5) or another mechanism (Sections 13.6 - 13.9). For those effects related to beam smearing, the uncertainties are found through computing $I(W)$ for the smeared beam. The fractional error for an individual harmonic is given by

$$\frac{\Delta(\delta T_l)}{\delta T_l} = \frac{1}{\delta T_l} \frac{\partial(\delta T_l)}{\partial \sqrt{I(W)}} = \frac{\delta \sqrt{I(W)}}{\sqrt{I(W)}}. \qquad (26)$$

The fractional error in groups of harmonics is smaller because the errors are computed for the highest harmonic in a band group, the one with the fewest number of physical beams between nulls in the synthesized beam and therefore the one most affected by beam smearing.

Errors are computed for D1, unless otherwise noted, because it has a smaller beam than D2 and is consequently more affected by smearing. Nominal values of $\sqrt{I(W)}$ are the following: $\sqrt{I(W)} = 0.377$ for D1 and $\sqrt{I(W)} = 0.350$ for D2 for the case of the 16-pt and 17-pt beams respectively.

Systematic Effect	Maximum Resultant Change in $\delta T/T$
Chopper jitter	$< 0.1\%$
Chopper zero offset drift	$< 0.2\%$
Miscalibration of chopper amplitude	$< 3\%$
Mis-calibration of azimuth	$< 0.1\%$
Mis-calibration of elevation	$< 1\%$
Incorrect determination of beam size	$< 1\%$
Electronic roll-off (between data points)	$< 0.2\%$
Gain variation in offsets	$< 3\%$
Chopper phase offset	$< 0.5\%$

TABLE 11

SYSTEMATIC EFFECTS

13.1. *Chopper Jitter*

Jitter in the chopper position, due to wind or electronic malfunction, smears the beam. All data for which the *rms* of the chopper position deviates more than $0.015°$ from the nominal position are rejected from the analysis. The maximum resulting error in either D1 or D2 in any harmonic (resulting from an increase in beam size in the direction parallel to the chop of $0.015°$) is $\delta\sqrt{I(W)} = -3.0 \times 10^{-4}$, or $\delta T_l/T_l \approx 0.1\%$.

13.2. *Chopper Zero Offset Stability*

Beam smearing can be caused by a drift in the electronic zero point of the chopping mirror. The zero point is monitored throughout the campaign. We find that from the beginning to the end of the analyzed data the zero drifts by $\approx 0°.03$. We can place an upper limit on the extent to which this can affect our result by considering a smearing of the beam in the direction parallel to the chop of $0°.03$. This results in $\delta\sqrt{I(W)} = -7 \times 10^{-4}$, or $\delta T_l/T_l \approx 0.2\%$.

13.3. *Mis-calibration of Azimuth*

If the azimuth changed over a period of time, the true beam could be uncertain by an amount equivalent to this change. The relative error in azimuth is $< 0°.01$ which could manifest itself as an increase in beam size in the direction parallel to the chop by a maximum of $0°.01$. The resultant errors are $\delta\sqrt{I(W)} = -2.0 \times 10^{-4}$, or $\delta T_l/T_l < 0.1\%$.

13.4. *Mis-calibration of Elevation*

Similarly, if the elevation changed over time, the true beam could be uncertain by an amount equivalent to this error. The relative error in elevation is $< 0°.01$ which could manifest itself as an increase in beam size in the direction perpendicular to the chop by a maximum of $0°.01$. The resultant errors are $\delta\sqrt{I(W)} = -3\times10^{-3}$, or $\delta T_l/T_l \approx 0.8\%$.

13.5. *Incorrect Determination of the Beam*

If the beam was incorrectly measured, there would be an effective beam smearing in either the direction parallel or perpendicular to the chop. Errors in the θ_{FWHM} of the beam are $\approx 0°.005$ and $\approx 0°.008$ for D1 and D2 respectively. The maximum resulting error in either channel in any harmonic is $\delta\sqrt{I(W)} = 2.5 \times 10^{-3}$, or $\delta T_l/T_l \approx 0.7\%$. This is an upper limit because errors in the determination of the beam affect the calibration as well and are therefore partially compensated.

13.6. *Mis-calibration of Chopper Amplitude*

If the chopper amplitude were mis-calibrated, the assumed number of physical beams fitting into a given synthesized beam could be wrong. We know the amplitude of the chopper to $< 2\%$ uncertainty (2σ). If the value used in the analysis were wrong by this amount, we find the resulting change, $\delta T_l/T_l < 3\%$ for the worst case harmonic. Most harmonics show a change of $\delta T_l/T_l < 1\%$. The entire spectrum also shifts a small amount in l. For a 2% increase in the chopper amplitude, we find $\approx 2\%$ shift in each point to lower l values. The sign of this effect is reversed if the chopper amplitude is smaller than the assumed value.

13.7. *Electronic Roll-off*

The likelihood contours shown in Figure 9 correspond to different post-detection frequencies as well as different l. The point at $l = 226$ contains data from the 6-pt to 7-pt beams in D1 and the 6-pt to 9-pt beams in D2 corresponding to $f \approx 25$ Hz. The point at $l = 409$ contains the 12-16-pt beams in D1 and 12-pt to 17-pt beams in D2, corresponding to $f \approx 50$ Hz. By calculation and measurement we show the electronic transfer function changes by $< 0.2\%$ over this range and thus does not affect the results.

13.8. *Gain Variation in the Offsets*

Variations in the cryogenic temperatures and the temperature of the warm electronics box lead to variations in the gain. If the effects of the decrease in gain of the warm amplifiers, the decrease in sensitivity of the SIS mixers, and the increase in output of the calibration source with increasing temperature are combined during the period of CMB observations, there could be an undetected gain drift of $\approx 1\%$. In addition, there could be other gain effects of order 3% that would escape detection because the variation in atmospheric opacity would mask their signature in the cal pulse. Because of the large heat capacity, such variations would occur on the time scale of hours.

Changes in gain affect the offset. Since the offsets are different for different synthesized beams, it is possible to

affect the spectrum through a gain change. When the average offsets for the combined harmonics are multiplied by a gain variation of $\approx 3\%$, a signal with amplitude $\approx 3\mu$K at low harmonics and $< 2\mu$K at higher harmonics results. Not only is this signal small, but it is largely accounted for through the offset and slope subtraction.

13.9. *Chopper Phase Offset*

If the phase of the chopper were to drift, the sky signal would be smeared because the beam would not be positioned according to the nominal chopper template. A cut is made that eliminates from the analysis all data for which the chopper amplitude differs from the *rms* average value by more than $0.015°$. This corresponds to a phase shift of 0.5 samples. A shift of this size contributes $< 0.5 \mu$ K in δT_l.

14. FOREGROUND EMISSION AND RESULTS

After the raw data have been reduced and binned on the sky, we determine the foreground emission contribution from our galaxy and from other galaxies. The foreground contribution at these frequencies, galactic coordinates, and angular scales is small (Tegmark *et al.* 2000; Coble *et al.* 1999; Masi *et al.* 2001). This is clear from Figure 10. The amplitude of the first peak is measured to be roughly the same from 30 to 144 GHz when the flux is expressed as changes in a 2.725 K thermal emitter. The spectral index of the fluctuations is $\beta_{CMB} = \ln(\delta T_{144}/\delta T_{36.5})/\ln(144/36.5) = -0.04\pm0.25$, where δT_{144} is the weighted mean of the two highest points for the D-band data and $\delta T_{36.5}$ is a similar quantity for the HEMT data (36.5 GHz is the average HEMT frequency). For the CMB, $\beta_{CMB} = 0$. For dust, $\beta_{RJ} = 1.7$ corresponds to $\beta_{CMB} = 2.05$; for free-free emission $\beta_{RJ} = -2.1$ corresponds to $\beta_{CMB} = -1.75$.

Fits to foreground templates were not done for Torbet *et al.* (1999) and Miller *et al.* (1999) and there was the possibility that the amplitude of the peak had a contribution from foreground emission (Page 2000; Knox & Page 2000). However, the mean frequency spectrum of the peak clearly singles out the CMB as the dominant source of the fluctuations. In addition, the angular spectra of the foreground emission is much different than that of measured angular spectrum of the CMB (Miller *et al.* 1999).

To quantify the foreground emission, we fit to four templates: the SFD dust map (Schlegel *et al.* 1997) (T_{SFD}), the Haslam synchrotron map (Haslam *et al.* 1982) (T_H), and the radio (T_{r-pt}) and IRAS (T_{ir-pt}) source compilations from the WOMBAT compilation (WOMBAT 2001). We have not yet fit to the H_α maps that trace microwave free-free emission. However, we note fits to SK (Gaustad *et al.* 1996; Simonetti *et al.* 1996) found that the free-free contribution was negligible. In addition, cross-correlations between the WHAM H_α maps (Haffner *et al.* 1999) and other CMB maps, including QMAP, do not show a significant contribution (de Oliveira-Costa *et al.* 2001).

There is a correlation between CMB maps at frequencies < 90 GHz and dust maps (Kogut 1996;

de Oliveira-Costa *et al.* 1997; Leitch *et al.* 1997). The mechanism responsible for the correlation is not yet certain (de Oliveira-Costa *et al.* 2001) though spinning dust grains is a strong candidate (Jones 1997; Drain & Lazarian 1998). The dust-correlated foreground component is larger than the free-free component traced by H_α between 20 and 40 GHz and is not correlated to the Haslam map (de Oliveira-Costa *et al.* 1998). Thus, the SFD map is a good tracer of foreground emission for the HEMT data. The galactic latitude of the CMB scan covers between $b = -8°$, $l = 280°$ and $b = -34°$, $l = 335°$ as shown in Figure 8. Our sky scan passes near the Large Magellanic Cloud (LMC, $b = -32°.9$, $l = 280°.5$) and we remove data near it. During the day, we observe known sources in the galactic plane (Puchalla *et al.* 2001).

The template fitting procedure is restricted to the section of sky analyzed for CMB anisotropy. The goal is to assess the contribution to the CMB results rather than to characterize foreground emission. First, the template map is multiplied by the synthesized beam in a manner such that the full CMB observing strategy is reproduced. Except in the case of the Haslam map for the $l > 200$ D-band data (where no correlation is expected), the size of the synthesized beam lobes is larger than the resolution of the template map. Next, for each harmonic, we fit to the template with

$$\chi^2 = \sum_{k=1}^{N_{n,bins}} \left(t_k - (a_0 T_{r-pt} + a_1 T_{ir-pt} + a_2 T_H + a_3 T_{SFD})\right)^2 w_k$$

(27)

where $N_{n,bins}$ is the number of filled bins around the sky for the $n-pt$ function ($< N_{RA}$, t_k is the CMB temperature (equation 24), and w_k is the statistical weight of each measurement. The fits are performed as a function of angular scale and frequency. Where the fit result is significant, as shown in Table 12, we subtract the foreground component in quadrature from δT_l as determined from the likelihood analysis[35].

The fit results may be summarized as follows: 1) The dominant source of contamination at 30 and 40 GHz is from the radio point sources as traced by the 4.85 GHz PMN catalog (Griffith & Wright 1993; Condon *et al.* 1993; Wright *et al.* 1994) on which the WOMBAT maps are based. The extrapolation to 30 GHz is known to be problematic because the source spectra vary from source to source (Puchalla *et al.* 2001). We cannot rule out a contribution from sources that are not traced by the extrapolated PMN survey but, because of the measured spectrum of the peak, such a contribution cannot be large. Over our sky coverage ≈ 600 deg^2, we account for ≈ 100 sources. Most of the contribution comes from the largest 10% and is spread throughout the observing region. 2) Contributions from synchrotron emission are negligible unless the synchrotron spectral index varies so much that the Haslam map is not a good template. The largest *rms* of the Haslam map, after applying the beam synthesis, is 0.6 K. When extrapolated to 30 GHz with a spectral index

---

[35] This simple treatment, where we ignore chance alignments of the CMB with the foregrounds [e.g., (de Oliveira-Costa *et al.* 1998)] and subtract the foreground in quadrature, is sufficient because the foreground contribution to the CMB $< 4\%$ in all cases. Future work will address the full treatment and the galactic plane.

TABLE 12
SUMMARY OF FOREGROUND CONTRIBUTIONS[a]

Foreground	$l = 60$[b]	$l = 85$	$l = 115$	$l = 150$	$l = 200$
IRAS sources at 30 GHz (μK)	$\cdots$	19	$\cdots$	$\cdots$	$\cdots$
Radio sources at 30 GHz (μK)	$\cdots$	16	23	16	13
Radio sources at 40 GHz (μK)	$\cdots$	11	10	$\cdots$	
SFD 30 GHz (μK)	18	$\cdots$	$\cdots$	$\cdots$	$\cdots$
SFD 40 GHz (μK)	$\cdots$	9	$\cdots$	$\cdots$	$\cdots$

[a]We do not give any value if the fitted foreground contribution is < 7 μK. At $l = 60$ this corresponds to a 1% correction and at $l = 200$ a 0.5% correction.
[b]The foreground contribution for a typical value of l.

of $\beta_{RJ} = -2.7$, one gets 5.5 μK, consistent with the fitted values. The fitted dust contribution at the 30 GHz $l = 60$ and 40 GHz $l = 80$ points, is small but consistent with the picture of 30 GHz dust-correlated emission. 3) There is no significant contamination at 144 GHz from either dust or point sources.

Table 13 gives the results from TOCO along with the revised results from QMAP and SK[36] based on foreground analyses and new information on the calibration. The final results for all three experiments are shown in Figure 10 along with a comparison to recent experiments.

15. DISCUSSION

Since the discovery of the anisotropy (Smoot *et al.* 1992), there have been many CMB anisotropy experiments at $l < 1000$ in addition to the ones noted thus far [ARGO (de Bernardis *et al.* 1994; Ratra *et al.* 1999), MSAM (Wilson *et al.* 1999), UCSB/SP (Gundersen *et al.* 1994), White Dish (Ratra *et al.* 1998), Python (Ruhl *et al.* 1995), BAM (Tucker *et al.* 1996), IAB (Piccirillo & Calisse 1993), Tenerife (Hancock *et al.* 1994), MAX (Lim *et al.* 1996)]. The SK experiment was the first to show the rise of the CMB angular spectrum in the region between $l = 50$ and $l = 250$ independent of any other experiment. At the time, the amplitude of the peak was considered high though consistent with the subsequently popular Λ-CDM models. Until TOCO, the SK spectrum was in mild conflict with other experiments.

Though a straightforward read of the data prior to TOCO suggested a peak at $l \approx 200$ [e.g., SK and OVRO (Leitch *et al.* 1998) or SK and CAT (Baker *et al.* 1999)] there were lingering questions of cross calibration and point source subtraction. In fact, if one did not include the SK data, the combined analysis of UCSB/SP, ARGO, MAX, White Dish, and SuZIE favored an open universe (Ratra *et al.* 1999b). Dodelson and Knox (2000) showed that TOCO alone singled out a flat universe as the best model. Others (Bahcall *et al.* 1999; Bond *et al.* 2000), including Dodelson and Knox, showed that the combination of all the data singled out a flat universe.

QMAP was designed to measure the anisotropy by direct mapping. Degree-resolution high signal-to-noise maps were made that could be compared to each other and, be-

cause they covered the same region of sky, confirmed the $l < 150$ Saskatoon results (Xu *et al.* 2000). The strategy of direct total power mapping was later employed by the BOOMERanG and MAXIMA experiments, which ushered in very high signal-to-noise sub-degree resolution mapping.

The TOCO experiment showed both the rise and fall of the first peak and showed its spectrum was that of the CMB with a single instrument (Figure 10). These results have since been amply verified by BOOMERanG, MAXIMA, and DASI. The rise to the maximum has high signal-to-noise; the fall for $l > 200$ is also clearly evident though worth quantifying. Miller *et al.* (1999) reported that the 95% upper limit of the last point in D-band, δT_{409}, was just below the 2σ lower bound of the point of the peak, δT_{226}. The penultimate point was not included in the assessment. Here we perform a more complete analysis. We focus on just the last three D-band points, δT_{226}, δT_{306}, δT_{409}, because the calibration uncertainty is common to all and drops out of the analysis. There are two ways a peak could be detected: $\delta T_{226} > \delta T_{409}$, and $\delta T_{306} > \delta T_{409}$ but with $\delta T_{409} \leq \delta T_{226}$. The net probability that a peak has been detected is given by the sum of the probabilities of these two possibilities.

We Monte Carlo the likelihood distributions to determine the above probabilities and to investigate the effects of correlations. We find $P(\delta T_{226} > \delta T_{409}) = 0.99614$ and $P(\delta T_{306} > \delta T_{409} | \delta T_{409} \leq \delta T_{226}) = 0.00369$. Thus, the net probability that a peak has been detected is 0.99983, or loosely speaking a $> 3.7\sigma$ detection. The correlations among these three points are positive and small, of order 0.01. When the correlations are accounted for, the net effect is to increase the significance of a detection of a peak. We emphasize that the detection is model independent, calibration independent, and conservative in the sense that if there is slight contamination by point-sources or there is some undetected source of correlation, the probability of the detection *increases*.

There are now many analyses that extract cosmological parameters assuming that the models from CMBFAST (Seljak & Zaldarriaga 1998) describe Nature, [e.g., (Bartlett *et al.* 1998; Lineweaver 1999; Tegmark & Zaldarriaga 2000; Jaffe *et al.* 2001)]. Here we compute δT_{peak} and l_{peak} directly from the data. This allows parameter estimation with the minimal amount

[36] In addition to some authors on this paper, SK was analyzed by Ed Wollack and Norm Jarosik.

TABLE 13
SUMMARY OF RESULTS FROM SK, QMAP, AND TOCO.

Experiment	l_e [a]	N_{n-pt} [b]	N_{bins} [c]	δT_l^{orig} [d] (μK)	δT_l^{fc} [e] (μK)	δT_l [f] (μK)	δT_l^2 (μK)^2
TOCO	63^{+18}_{-18}	2	16,20	$39.7^{+10.3}_{-6.5}$	35.4	$35.1^{+10.2}_{-6.4}$	1232^{+820}_{-408}
QMAP	80^{+41}_{-41}	$\cdots$	$\cdots$	47^{+6}_{-7}	46.0	$48.3^{+6.4}_{-7.5}$	2401^{+668}_{-679}
TOCO	86^{+16}_{-22}	3	17-28	$45.3^{+7.0}_{-6.4}$	43.4	$43.0^{+6.9}_{-6.3}$	1846^{+644}_{-499}
SK	87^{+39}_{-27}	15	24,48	49^{+8}_{-5}	48.0	$50.2^{+8.3}_{-5.2}$	2520^{+902}_{-495}
QMAP	111^{+64}_{-64}	$\cdots$	$\cdots$	52^{+5}_{-5}	52.0	$54.6^{+5.3}_{-5.3}$	3069^{+615}_{-559}
TOCO	114^{+20}_{-24}	6	22-42	$70.1^{+6.3}_{-5.8}$	68.0	$67.3^{+6.3}_{-5.8}$	4529^{+888}_{-747}
QMAP	126^{+54}_{-54}	$\cdots$	$\cdots$	59^{+6}_{-7}	58.0	$60.9^{+6.4}_{-7.5}$	3819^{+832}_{-871}
TOCO	128^{+26}_{-33}	1	84	$54.6^{+18.4}_{-16.6}$	54.6	$53.7^{+18.1}_{-16.3}$	2884^{+2272}_{-1485}
TOCO	152^{+28}_{-38}	3	84	$82.0^{+11.0}_{-11.0}$	82.0	$80.6^{+10.8}_{-10.8}$	6497^{+1858}_{-1625}
TOCO	158^{+22}_{-23}	6	29-55	$88.7^{+7.3}_{-7.2}$	87.2	$86.4^{+7.2}_{-7.1}$	7465^{+1296}_{-1177}
SK	166^{+30}_{-43}	10	48,96	69^{+7}_{-6}	67.6	$70.5^{+7.3}_{-6.2}$	4970^{+1080}_{-836}
TOCO	199^{+38}_{-29}	11	54-82	$84.7^{+7.7}_{-7.6}$	83.7	$82.9^{+7.6}_{-7.6}$	6872^{+1318}_{-1202}
TOCO	226^{+37}_{-56}	6	125	$83.0^{+7.0}_{-8.0}$	83.0	$81.6^{+6.9}_{-7.9}$	6659^{+1174}_{-1094}
SK	237^{+29}_{-41}	4	48,96	85^{+10}_{-8}	83.3	$86.8^{+10.4}_{-8.3}$	7535^{+1914}_{-1372}
SK	286^{+24}_{-36}	4	48,96	86^{+12}_{-10}	84.3	$87.9^{+12.5}_{-10.4}$	7726^{+2354}_{-1720}
TOCO	306^{+44}_{-59}	6	165	$70.0^{+10.0}_{-11.0}$	70.0	$68.8^{+9.8}_{-10.8}$	4733^{+1445}_{-1369}
SK	349^{+44}_{-41}	5	48,96	69^{+19}_{-28}	67.6	$70.4^{+19.8}_{-29.1}$	4956^{+3180}_{-3275}
TOCO [g]	409^{+42}_{-65}	9	250	< 67 (95%conf)	$\cdots$	$23.3^{+22.4}_{-22.4}$	545 ± 2043

[a] l_e is computed from the window function or the Knox filter following Bond (1994). In practice, we find little difference between the combined weighted windows (Netterfield *et al.* 1997) and Knox filters (Knox 1999).

[b] The total number of individual n-pt functions combined in the covariance matrix **M**. We emphasize that all known correlations are accounted for. For QMAP, n-pt functions correspond to different eigenmodes for the map.

[c] The number of data points or RA bins. When two numbers or a range are given, not all n-pt beams have the same RA bins.

[d] The originally published values following the convention in Netterfield *et al.* (1997). Calibration error is not included.

[e] The original value corrected for foreground emission (fc) . For SK, (de Oliveira-Costa *et al.* 1997) found a $\approx$ 2% contamination of the data due to a foreground component correlated with dust emission. For QMAP a similar correction was found (de Oliveira-Costa *et al.* 1999). The entries show the spectrum after the corrections. The corrections are done separately for Ka and Q bands before they are combined.

[f] The foreground and calibration corrected values. The recalibration is based on new information about the calibration sources or, in the case of TOCO, on a 1-2% correction for the electronic bandpass. After SK data were published, (Mason *et al.* 2000) reported a more accurate calibration of Cas-A, which we used for QMAP. This led to an increase of 4% for the SK data and a reduction in the calibration error from 14% to 10%. There is also a small correction to put the results in the $l(l + 1)/2\pi$ format as opposed to the $l(2l + 1)/4\pi$. Calibration error is not included.

[g] Originally, the 95% upper limit and likelihood curves were given for this bin whereas 1σ error bars were plotted for the other points. We here adopt the convention in Mauskopf *et al.* (2000), and give all results with 1σ error bars. The data are the same as before (Miller *et al.* 1999) except for the 1.7% calibration correction. The likelihood distribution is not Gaussian. The value of 23 ± 22 μK matches the distribution in the sense that the likelihood peak is at 23 μK and $\approx$ 95% of the probability is $< 67 = 23 + 2\sigma$ μK. The value of 545 ± 2043 $(\mu K)^2$ comes from fits to the likelihood following Bond *et al.* 2000 and is often used to represent the likelihood. Note that $\sqrt{545 + 2\sigma} = 68$ μK. We set the error bar on δT_l by forming $(\sqrt{545 + 2\sigma} - \sqrt{545})/2$. μK. For detailed analyses, the full likelihood as shown in Figure 9 should be used.

FIG. 10.— The combination of the SK, QMAP, and TOCO data with all corrections. Following Netterfield *et al.* (1997), we plot the position of the maximum of the likelihood with error bars that encompass 68.3% of the likelihood for all points where there is a significant detection. For the last TOCO point we plot a representation of 1σ based on Bond *et al.* (2000). The plot is made with δT as opposed to δT^2 because δT directly shows the signal-to-noise. For example, $\delta T = 5 \pm 1$ μK has a S/N = 5 whereas the equivalent $\delta T = 25 \pm 10$ μK has an apparent S/N $\approx$ 3. The models are "standard CDM" (lower) and the best fit from Jaffe *et al.* (2000) (upper). Calibration error is not included.

of model dependence. From the TOCO and SK data,   the average amplitude of the peak between $l = 160$ and

$l = 240$ is $\delta T_{peak} = 80.9 \pm 3.4 \pm 5.1$ μK where the first error is statistical and second error is for calibration (the 1 μK shift from (Miller *et al.* 1999) is mostly due to the new calibration). Following Knox and Page (2000), we find $l_{peak} = 216 \pm 14$ in a relatively model independent parametrization [37].

The SK, QMAP, and TOCO experiments used a variety of techniques, separate data reduction and analysis pipelines, and two different calibrators. These different experiments, rich with consistency checks, trace out a peak. We have described the systematic checks, focusing on the TOCO data, and have not found any instrumental effect or data reduction artifact that could mimic or produce the signal we see. It is possible that extragalactic sources with spectra different from the ones we assume could alter our results but the effect would be small and accounting for it would tend to enhance the downturn for $l > 220$. In conclusion, these experiments, in particular the TOCO experiment, have measured the rise, amplitude, position, and fall of the first peak in the angular spectrum of the CMB.

REFERENCES

Baars, J. W. M., Genzel, R., Pauliny-Toth, I. I. K., & Witzel, A. 1977, A&A, 61, 99

Bahcall, N., Ostriker, J. P., Perlmutter, S., & Steinhardt, P. J. 1999, Science, 284, 1481 (astro-ph/9906463)

Baker, J. C *et al.* 1999, MNRAS, 308, 1173 (astro-ph/9904415)

Bartlett, J. G., Blanchard, A., Douspis, M., & Le Dour, M. 1998, in Proc Evol of Large Scale Structure (Garching) (astro-ph/9810318)

Blundell, R., Miller, R. E., & Gundlach, K. H. 1992, Int J of Infrared and Millimeter Waves, 13, 1

Bock, J., Glenn, J., Grannan, S., Irwin K., Lange A., LeDuc H., & Turner, A. 1998, in Proc. of SPIE, 3357 Advanced Technology MMW, Radio, and Terahertz Telescopes, ed. T.G. Phillips (Kona, Hawaii), 26

Bond, J. R., Crittenden, R., Davis, R. L., Efstathiou, G., & Steinhardt, P. J. 1994, PRL, 72, 1, 13

Bond, J. R. 1995, Astro. Lett. & Comm. 32, 1

Bond, J. R. 1996, in Cosmology and Large-Scale Structure, Les Houches Session LX, Theory and Observations of the Cosmic Microwave Background Radiation, ed. R. Schaeffer (Elsevier Science Press)

Bond, J. R., Jaffe, A. H., & Knox, L. 1998, Phys. Rev. D, 57, 2117

Bond, J. R., Jaffe, A. H., & Knox, L. 2000, ApJ, 533, 19 (astro-ph/9808264)

Chini, R., Kreysa, E., Mezger, P. G., & Gemünd, H. P. 1984, A&A, 137, 117

Clarricoats, P. J. B., & Olver, A. D. 1984, Corrugated Horns for Microwave Antennas (London: Peter Peregrinus).

Coble, K. *et al.* 1999, ApJ, 519, L5 (astro-ph/9902195)

Condon, J. J., Griffith, M. R., Wright, A. E. 1993, AJ, 106 1095

Cornish, N., 2000, (astro-ph/0005261)

Cortiglioni, S. 1994, Rev. Sci. Instrum., 65, 8, 2667

Cottingham, D. 1987, *A Sky Temperature Survey at 19.2 GHz Using a Balloon Borne Dicke Radiometer for Anisotropy Tests of the Cosmic Microwave Background*, PhD Thesis, Princeton University

de Bernardis, P. *et al.* 1994, ApJ, 422, L33

de Bernardis, P. *et al.* 2000, Nature, 404, 6781, 955

de Bernardis, P. *et al.* 2001, ApJ, in press (astro-ph/0105296)

de Oliveira-Costa, A., Kogut, A., Devlin, M. J., Netterfield, C. B., Page, L. A., & Wollack, E. J. 1997, ApJ, 482, L17

de Oliveira-Costa, A., Devlin, M. J., Herbig, T. H., Miller, A. D., Netterfield, C. B., Page, L. A. & Tegmark, M. 1998, ApJ, 509, L77

de Oliveira-Costa, A., Tegmark, M., Page, L. A., Boughn, S. 1998, ApJ, 509, L9

de Oliveira-Costa *et al.* 1999, ApJL, 527, L9-L12 (astro-ph/9904296)

de Oliveira-Costa, *et al.* 2001, astro-ph/0010527

Drain, B. T., & Lazarian, A. 1998, ApJ, 494, L19

Devlin, M. J., de Oliveira-Costa, A., Herbig, T., Miller, A. D., Netterfield, C. B., Page, L. A., & Tegmark, M. 1998, ApJ, 509, L73

Dicke, R. H., 1946, Rev. Sci, Instr., 17, 268

Dodelson, S. & Knox, L. 2000, Phys. Rev Lett., 84, 3523 (astro-ph/909454)

Doroshkevich, A. G., Zel'dovich, Ya. B. & Sunyaev, R. 1978, Sov. Astron. 22, 5

Downey, P. *et al.* 1984, AO 23, 910

Fixsen, D. *et al.* 1996, ApJ, 470, 63

Fixsen, D., Hinshaw, G., Bennett, C. L., Mather, J. C. 1997, ApJ, 486, 623 (astro-ph/9704176)

Ganga, K. M. *et al.* 1993, ApJ432, L15

Gaustad, J. E., McCullough, P. R., Van Buren, D. 1996, PASP, 108, 351

Griffin, M. J., Ade, A. R., Orton, G. S., Robson, E. I., Gear, W. K., Nolt, I. G., & Radostitz, J. V. 1986, Icarus, 65, 244

Griffith, M. R. & Wright, A. E. 1993, AJ 105, 1666

Gundersen, J. *et al.* 1994, ApJ, 433, L57 (astro-ph/9412020)

Haffner, L. M., Reynolds, R. J., & Tufte, S. L. 1999, ApJ, 523, 223

Halverson, N. *et al.* 2001, ApJ, in Press (astro-ph/0104489)

Hanany, S. *et al.* 2000, ApJ, 545, 5 (astro-ph/0005123)

[37] The peak value from this method, $\delta T_{peak} = 86 \pm 8$ μK, is sensitive to the type of fit whereas l_{peak} is relatively fit-independent. We prefer the straightforward average as it is computed directly from the data.
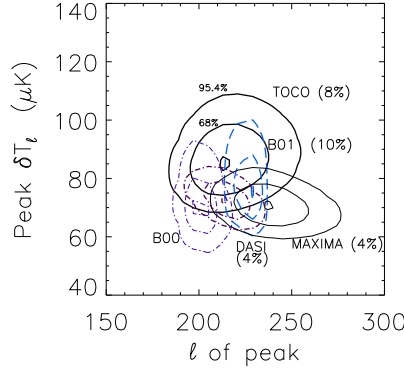
FIG. 11.— We show the position and amplitude of the first peak following the Gaussian Temperature method (Knox & Page 2000). For TOCO $l_{peak} = 216 \pm 14$ and $\delta T_l = 86 \pm 8$ μK. These values are slightly different than those reported before ($l_{peak} = 212$ and $\delta T_l = 88$ μK) because the of the calibration and foreground corrections. The preliminary BOOMERanG (de Bernardis *et al.* 2000) data give $l_{peak} = 201$ and $\delta T_l = 70$ μK; the reanalyzed and expanded data set (Netterfield *et al.* 2001) gives $l_{peak} = 226$ and $\delta T_l = 77$ μK. (We omit the North American Flight.) The BOOMERanG beam error is not accounted for; it will tend to broaden the distribution in l. MAXIMA (Lee *et al.* 2001) yields $l_{peak} = 238$ and $\delta T_l = 71$ μK and DASI (Halverson *et al.* 2001) gives $l_{peak} = 213$ and $\delta T_l = 74$ μK. These values are close ($< 1\sigma$) to the values found in de Bernardis *et al.* (2001) using different methods. Calibration error has been taken into account though the correlations between bands have not. When treated consistently, TOCO, B01, MAXIMA, and DASI pick out values for the peak position and amplitude that are within 2σ of each other.

Hancock, S., Davies, R. D., Lasenby, A. N., Guiterrez de La Cruz, C. M., Watson, R. A., Rebolo, R., & Beckman, J. E. 1994, Nature, 367, 333
Harrison, D. L., *et al.*, 2000, MNRAS, 316, 624
Haslam, C. G. T., Stoffel, H., Salter, C. J., & Wilson, W. E. 1982, A&AS, 47, 1
Herbig, T., Devlin, M. J., de Oliveira-Costa, A., Miller, A. D., Page, L. A., & Tegmark, M. 1998, ApJ, 509, L73
Hivon, E., Gorski, K. M., Netterfield, C. B., Crill, B. P., Prune, S., & Hansen, F. 2001, ApJ, in Press (astro-ph/0105302)
Hobson, M. P., Lasenby, A. N., & Jones, M. 1995, MNRAS 275, 863
Hu, W. and White, M. 1996, ApJ, 471, 30
Jaffe, A. *et al.* 2001, PRL, 86, 3475
James, G. L., & Thomas, B. M. A. 1982, IEEE Trans. Microwave Theory Tech., MTT-30, 3, 278.
Jarosik, N. 1996 IEEE MTT, 44, 2, 193
Jones, W. C. 1997, *A New Component of Galactic Emission*, Junior Paper, Princeton University.
Jungman, G., Kamionkowski, M., Kosowsky, A., & Spergel, D. N. 1995, Phys. Rev. D., 54, 1332
Kamionkowski, M. *et al.* 1994, astro-ph/94010003.
Kogut, A., Banday, A. J., Bennett, C. L., Gorski, K. M., Hinshaw, G., & Reach, W. T. 1996, ApJ, 460, 1
Keller, J., 1962, Geometrical Theory of Diffraction, Journal of the Optical Society of America, 52, 2, 116
Kerr, A. R., Pan, S. K., Lichtenberger, A. W., Lloyd, F. L., & Horner, N. 1993, in Proceedings of the Fourth International Symposium on Space Terahertz Technology, A New SIS Mixer for the 2-mm Band
Kerr, A. R., Feldman, M. J., & Pan, S. K. 1997, in Proceedings of the Eighth International Symposium on Space Terahertz Technology, Receiver Noise Temperature, the Quantum Noise Limit, and the Role of the Zero-Point Fluctuations
Knox, L. 1995, Phys.Rev. D, 52, 4307 (astro-ph/9504054)
Knox, L. 1999, Phys.Rev. D, 60, 103516, (astro-ph/9902046)
Knox, L. & Page, L. 2000, PRL, 85, 1366 (astro-ph/0002162)
Landau, L. D. & Lifshitz, E. M. 1960, Electrodynamics of Continuous Media (Pergamon)
Lee, A., Richards, P., Nam, S., Cabrera, B., & Irwin, K. 1996, APL, 69, 1801
Lee, A. T. *et al.* 2001, (astro-ph/0104459)
Leitch, E. M., Readhead, A. C. S., Pearson, T. J., & Myers, S. T. 1997, ApJ, 486, L23
Leitch, E. M., Readhead, A. C. S., Pearson, T. J., Myers, S. T., Gulkis, S., & Lawrence, C. R. 1998, ApJ, 532, 37
Leitch, E. M. *et al.* 2001, ApJ, in Press (astro-ph/0104488)
Lim *et al.* 1996, ApJ, 469, L69
Lineweaver, C. H. 1999, Science, 284, 1503 (astro-ph/9909301)
MacA Thomas, 1978, IEEE Trans. on Ant. and Prop, AP-26, 2
Mason, B. S., Leitch, E. M., Myers, S. T., Cartwright, J. K., & Readhead, A. C. S. 1999, AJ, 118, 2908 (astro-ph/9903383)
Masi *et al.* 2001 (astro-ph/0101539)
Mauskopf, P. *et al.* 2000, ApJ, 536, L59 (astro-ph/9911444)

Mezger, P. G., Tuffs, R. J., Chini, R., Kreysa, E., & Gemünd, H. P. 1986, A&A, 167, 145
Miller, A. *et al.* 1999, ApJ, 524, L1
Monnelly, G. P. 1996, Senior Thesis, Princeton University
Netterfield, C. B., Jarosik, N., Page, L., Wilkinson, D., & Wollack, E. J. 1995, ApJ, 445, L69
Netterfield, C. B., Devlin, M. J., Jarosik, N., Page, L., & Wollack, E. J. 1997, ApJ, 474, 47
Netterfield C. B. *et al.* 2001, (astro-ph/0104460) ApJ, in press
Padin, S. 2001, ApJ, 549, L1 (astro-ph/0012211)
Page, L., astro-ph/9911199 Proceedings from the Newton Institute's "Structure Formation in the Universe" conference, Sept, 1999. Organizers: VA Rubakov, PJ Steinhardt, & N. Turok
Park, C.-G., Park, C., Ratra, B., & Tegmark, M. 2001, ApJ, in Press (astro-ph/0102406)
Partridge, R. B., 1995, 3K: The Cosmic Microwave Background Radiation, (Cambridge:Cambridge University Press)
Peterson, J. B. *et al.* 2000, ApJ, 532, 2, L83 (astro-ph/9910503)
Piacentini, F. *et al.* 2001, ApJ, in Press (astro-ph/0105148)
Piccirillo, L. & Calisse, P. 1993, ApJ, 413, 529
Pospieszalski, M. W. 1989, Proc. IEEE Microwave Theory Tech., 37, 1340
Pospieszalski, M. W. 1992, Proc. IEEE Microwave Theory Tech., MTT-S 1369; and Pospieszalski, M. W. 1997, Microwave Background Anisotropies, ed F. R. Bouchet (Gif-sur-Yvette: Editions Frontièrs), 23
Pospieszalski, M. W. *et al.* 1994, IEEE Microwave Theory Tech., MTT-S Digest, 1345
Pryke, C. *et al.* 2001 (astro-ph/0104490)
Puchalla, J. L. *et al.* 2001, Astronomical Journal, in Press (astro-ph/0005420)
Ratra, B., Ganga, K., Sugiyama, N., Tucker, G. S., Griffin, H. T., Nguyen, J. B., & Peterson, J. B. 1998, ApJ, 505, 8 (astro-ph/9710270)
Ratra, B., Ganga, K., Stompor, R., Sugiyama, N., de Bernardis, P., & Górski, K. M. 1999, ApJ, 510, 11
Ratra, B., Stompor, R., Ganga, K., Rocha, G., Sugiyama, N., & Górski, K. M. 1999, ApJ, 517, 549 (astro-ph/9901014)
Romeo, G., Ali, S., Femenia, B., Limon, M., Piccirillo, L., Rebolo, R., & Schaefer, R. 2000, ApJ, in Press (astro-ph/0011226)
Robertson, T. L., 1996, Development of a 144 GHz Cryogenic Heterodyne Radiometer Based on SIS Junctions, Senior Thesis, Princeton University
Ruhl, J. E., Dragovan, M., Platt, S. R., Kovac, J., & Novak, G. 1995, ApJ, 453, L1
Schlegel, D. J., Finkbeiner, D. P., & Davis, M. 1997, ApJ, 500, 525 (astro-ph/9710327)
Seljak, U., & Zaldarriaga, M. 1998 and 1996, ApJ, 469, 437. The CMBFAST code is available through http://www.sns.ias.edu/matiasz/CMBFAST/cmbfast.htm
Simonetti, J. H., Dennison, B., & Topansa, G. A. 1996, ApJ, 458, L1
Smoot, G. F. *et al.* 1992, ApJ, 396, L1

Staren, J. *et al.* 2000, ApJ, 539, 52 (astro-ph/9912212)

Tegmark, M. 1997, Phys. Rev. D, 56, 4514 (astro-ph/9705188)

Tegmark, M., de Oliveira-Costa, A., Devlin, M., Netterfield, C. B., Page, L. & Wollack, E. 1997, ApJ, 474, L77 (astro-ph/9608018)

Tegmark, M., 1999, ApJ, 514, L69 (astro-ph/9809201)

Tegmark, M., Eisenstein, D., Hu, W., & de Oliveira-Costa, A. 2000, ApJ, 530, 133 (astro-ph/9905257)

Tegmark, M., & Zaldarriaga, M. 2000, Phys. Rev. Lett., 85, 2240 (astro-ph/0004393)

The TopHat experiment: http://topweb.gsfc.nasa.gov/index.html

Torbet, E. *et al.* 1999, ApJ, 521, L79 (astro-ph/9905100)

Tucker, J., & Feldman, M. J. 1985, Reviews of Modern Physics, 57, 4

Tucker, G. S. 1991, An Instrument to Search for Small Scale Anisotropy in the Cosmic Microwave Background at 90 GHz, Ph.D. thesis, Princeton University

Tucker, G. S., Gush, H. P., Halpern, M., Shinkoda, I., & Towlson, W. 2000, ApJ, 475, L73 (astro-ph/9611225)

Ulich, B. L. 1981, Astr. J., 86, 11, 1619

Wang, X., Tegmark, M. & Zaldarriaga, M. Submitted to PRD (astro-ph/0105091)

Weiss, R. 1980, Ann. Rev. Astron Astrophys., 18, 489

White, M., Carlstrom, J., Dragovan, M., & Holzapfel, W. 1999, ApJ, 514, 12 (astro-ph/9712195)

Wilson, G. W. *et al.* 2000, ApJ, 532, 57 (astro-ph/9902047)

Wollack, E. J., Jarosik, N., Netterfield, C. B., Page, L., & Wilkinson, D. 1993, ApJ, 419, L49

Wollack, E. J. 1994, PhD Thesis, Princeton University

Wollack E. J. 1995, RSI, 66, 8, 4305-4312

Wollack, E. J., Devlin, M. J., Jarosik, N. J., Netterfield, C. B., Page, L., Wilkinson, D. 1997, ApJ, 476, 440

Wollack, E. J., & Pospieszalski, M. W. 1998, Characteristics of Broad-Band InP Millimeter-Wave Amplifiers for Radiometry, IEEE MTT-S International Microwave Symposium Digest, 669

WOMBAT home page: http://astron.berkeley.edu/wombat/

Wright E. 1996, IAS CMB Data Analysis Workshop (Princeton) (astro-ph/9612006)

Wright, A. E., Griffith, M. R., Burke, B. F., & Ekers, R. D. 1994, ApJ, 91, S111

Xu, Y., Tegmark, M., de Oliveira-Costa, A. Devlin, M. J., Herbig, T., Miller, A. D., Netterfield, C. B., Page, L., 2000, PRD, 63, 103002 (astro-ph/0010552)

Xu, Y., Tegmark, M., & de Oliveira-Costa, A. 2001, PRD, in Press (astro-ph/0104419)

YRS Associates: Rahmat-Samii, Y., Imbriale, W., & Galindo, V., 4509 Tobias Ave. Sherman Oaks, CA 91403